Mechanical modelling of viscoelastic hierarchical suture joints and their optimisation and auxeticity

F. Ongaro[a], N.M. Pugno[a,b,1]

[a] Laboratory for Bio-inspired, Bionic, Nano, Meta Materials & Mechanics, Department of Civil, Environmental and Mechanical Engineering, University of Trento, 38123 Trento, Italy [b] School of Engineering and Materials Science, Queen Mary University of London, Mile End Road, London E1 4NS, United Kingdom

ARTICLE INFO

Keywords:
Viscoelasticity
Hierarchy
Suture joints
Effective properties
Loss factor
Auxeticity

ABSTRACT

It has been widely recognised that suture joints play a fundamental role in the exceptional mechanical properties of many biological structures like the cranium and ammonite fossil shells. Up to date, many efforts have been devoted to investigate suture interfaces to predict the relations between the characteristics of its two phases, the teeth and the interface layer, and the structure effective properties. However, in very few works the viscoelasticity of the suture components has been taken into account. To provide a contribution in this limitedly explored research area, this paper describes the mathematical formulation and modelling technique leading to explicit expressions for the effective properties of viscoelastic suture joints with a general trapezoidal waveform. It emerges a strong influence of the suture geometric and mechanical characteristics on the effective properties and a parametric analysis reveals that an auxetic behavior can be obtained simply by tailoring the suture parameters. The effects of adding hierarchy into the above system are also explored and closed-form relations for the effective moduli are derived. Optimal levels of hierarchy can be identified and, similarly to the non-hierarchical case, an auxetic behavior emerges for particular values of the suture parameters. Finally, an extension of the theory to the sinusoidal sutures in biology is reported. By considering the examples of the cranium and the woodpecker beak, it emerges that the first is optimised to obtain high stiffness, while the second to obtain high energy dissipation levels.

1. Introduction

Received 4 August 2022; Received in revised form 16 August 2023; Accepted 29 August 2023 Available online 6 September 2023

Suture joints with different geometries are commonly found in biology from the micro- to the macro-length scales. Examples include the carapace of the turtle (Krauss et al., 2009; Damiens et al., 2012), the woodpecker beak (Lee et al., 2014), the cranium (Pritchard et al., 1956), the seedcoat of the *Portulaca oleracea* (Gao et al., 2018a) and *Panicum miliaceum* (Lu et al., 2009) and ammonite fossil shells (Li et al., 2012), among others. The suture joint architecture, where two interdigitating stiff components (the teeth) are joined by a thin compliant seam (the interface layer), allows an high level of flexibility and is the key factor for the accomplishment of biological vital functions such as respiration, growth, locomotion and predatory protection (Jaslow and Biewener, 1995; Jaslow, 1990; Farr, 2007). From a mechanical point of view, it has computationally and/or experimentally been demonstrated that this particular configuration endows an excellent balance of stiffness, strength, toughness, energy dissipation and a more efficient way to bear and transmit loads (Li et al., 2013; Yu et al., 2020; Gao et al., 2018b; Ghazlan et al., 2015; Gao and Li, 2019a). Emblematic is the case of the leatherback sea turtle, a unique specie of sea turtle having the capacity to dive to a depth of 1200 m (Chen et al., 2015). As reported in Chen et al. (2015), this is due to the particular design of the turtle carapace, where an assemblage of bony plates interconnected with collagen fibres in a suture-like arrangement is covered by a soft and stretchable skin. The combination of this two elements provides a significant amount of flexibility under high hydrostatic pressure, as well as exceptional mechanical functionality in terms of stiffness, strength and toughness, being the collagenous interfaces an efficient crack arrester. These fascinating performances, however, are strongly affected by the suture geometry that, in nature, varies among and within species as a result of an evolutionary process (Allen, 2007; De Stefano et al., 2009; Song et al., 2010). This is confirmed in Jaslow (1990), Jasinoski et al. (2010), where it emerges that an increased level of interdigitation found in the cranial sutures of different mammalian species leads to an increase in the suture bending strength and energy storage (Jaslow, 1990; Jasinoski et al., 2010). Similarly, De Blasio (2008) explains not only how the high sinuosity and complexity of the suture lines in ammonites are the result of an evolutionary response to the hydrostatic pressure, but also that the stresses, displacements and deformations significantly decrease with the level of complexity. Analogous results are obtained in Pérez-Claros et al. (2002), which seeks to clarify the functional significance of the complex suture pattern in ammonites by means of a fractal analysis-based technique. The geometric characterisation of different types of biological suture joints is also reported in Saunders (1999), Hubbard and Melvin (1971) and Hartwig (1991).

Starting from the pioneering contributions in Saunders (1999), Hubbard and Melvin (1971), Hartwig (1991), De Blasio (2008) and PérezClaros et al. (2002), many authors studied the mechanics of suture joints and a vast literature has flourished in recent years. Simple relations between the geometric parameters (tooth shape, tooth tip angle, volume fraction of the teeth) and effective mechanical properties (stiffness, strength, fracture toughness) of trapezoidal suture joints are reported in Li et al. (2013, 2011), together with a discussion on the role of geometry on the suture mechanical behavior. Experimental results are illustrated in Lin et al. (2014), Cao et al. (2019), Malik and Barthelat (2016) and Malik et al. (2017) for the characterisation of the deformation and failure mechanism of 3D-printed suture joints with different geometries. An enhancement in the overall toughness and load-bearing capacity have been observed in the case of a sinusoidal waveform, suggesting a possible way to improve suture joints where the major structure is made of a brittle polymer (Cao et al., 2019). An application of the theory in Li et al. (2013, 2011) to the wavypatterned sutures of the common millet (*Panicum miliaceum*) seedcoat is discussed in Hasseldine et al. (2017) and Gao and Li (2019a), where the important role played by suture interfaces in resisting indentation loads is revealed (Hasseldine et al., 2017). Inspired by the hierarchical suture joints found in ammonite fossil shells, the authors of Li et al. (2012) propose a two-dimensional deterministic fractal model to investigate the role of hierarchy on the stiffness, strength and failure mechanism of triangular sutures. The hierarchical configuration, in particular, is obtained by superimposing a self-similar waveform with a shorter wavelength on each wave of the former profile.

[1] Corresponding author.
E-mail addresses: federica.ongaro@unitn.it (F. Ongaro), nicola.pugno@unitn.it (N.M. Pugno).
https://doi.org/10.1016/j.mechmat.2023.104785

An increasingly complex suture pattern is thus created and, in line with Li et al. (2013, 2011), an energetic approach leads to analytical relation between its effective properties and its geometric and mechanical features. More recently, a multiscale fracture analysis of staggered composites consisting of wave tablets is proposed in Liu and Wei (2021), where the influence of the tablets waveform on the effective fracture resistance and damage tolerance is clarified. Finally, the analysis of the damping performances of viscoelastic composites with sutural interfaces is presented in Yu et al. (2020), where closed-form expressions for the loss factor, loss modulus and storage modulus are reported for the case of triangular and trapezoidal sutures.

As clearly emerges, in the literature many works are devoted to the mechanical characterisation of suture joints, with a special attention on the role of the suture geometry on the overall behavior. Surprisingly, in spite of the proven benefits distinguishing the biological hierarchical sutures, very few investigations are currently available on this topic. In addition, very few investigations concern suture joints where one or both phases display a viscoelastic material response. To make a contribution to this incomplete research area and to provide some useful tools for practical applications, this paper focuses on the effects of adding hierarchy into a two-dimensional viscoelastic suture joint having a general trapezoidal configuration. The work is organised in 8 sections, including this introduction. Initially, based on the elastic–viscoelastic correspondence principle, Section 2 illustrates the mathematical formulation and modelling technique leading to closed-form relations for the effective moduli (Young's moduli, shear modulus and Poisson's ratios) and damping properties (loss factor, storage moduli and loss moduli). Considerations about the influence of the suture geometric and mechanical characteristics on the effective properties are presented in Section 3. In Section 4, the theory is extended to hierarchical sutures and explicit expressions for the effective viscoelastic properties are derived. A parametric analysis to investigate how the effective behavior is affected by the suture features in the hierarchical case is summarised in Sections 5 and 6. Optimal levels of hierarchy can be identified, together with the possibility to achieve auxeticity for particular suture configurations. As a real-case example, Section 7 illustrates the extension of the model to evaluate the effective stiffness and damping properties of the sinusoidal patterned sutures in biology. Two cases are compared: the cranium and the woodpecker beak. The first is found to be optimised for obtaining high stiffness, the second for obtaining high energy dissipation levels. As a conclusion, Section 8 summarises the main findings. To the authors best knowledge, this study is the first to explore a suture joint by incorporating both the two fundamental ingredients of hierarchy and viscoelasticity.

2. Viscoelastic suture joints: theoretical description and effective properties

2.1. Problem statement: basic concepts and assumptions

From a mechanical point of view, suture joints can be represented as a composite material including two interdigitating stiff phases (the teeth) joined by a thin compliant element (the interface layer) along the seam line (Fig. 1). Due to physiological reasons as respiration, growth or motion of the biological system (Li et al., 2013), suture joints are( ) often subjected to a in-plane far-field external tension $\hat{\boldsymbol{\sigma}} = \hat{\sigma}_{11}\, \hat{\sigma}_{22}\, \hat{\sigma}_{12}$ acting along the far-field boundaries $\partial\Omega$ (Fig. 1a). These loads are transmitted across the interface through a combination of interfacial shear and normal stresses given, respectively, by

$$\begin{cases} \tau_I = \tau_I\left(\hat{\sigma},\, \alpha_S,\, \beta_S,\, \vartheta_S\right) \\ \sigma_I = \sigma_I\left(\hat{\sigma},\, \alpha_S,\, \beta_S,\, \vartheta_S\right) \end{cases} \tag{1}$$

with α_S, β_S, ϑ_S the geometric parameters defining the interface profile (Figs. 1c, 2).

If we impose the equilibrium conditions at the interface, it emerges that the tangential and normal components of stress within the two phases satisfy the following relation (Fig. 1b):

$$\begin{cases} \tau_T = \tau_L = \tau_I \\ \sigma_T = \sigma_L = \sigma_I, \end{cases} \tag{2}$$

being $(\cdot)_T$ and $(\cdot)_L$, on order, the stresses within the teeth and the interface layer. In line with Li et al. (2013), the effective mechanical properties of suture joints can be obtained by focusing on the interdigitating area (Fig. 1c), whose boundaries are now coinciding with $\partial\Omega$, where the tension $\hat{\boldsymbol{\sigma}}$ is applied. Also, due to the periodicity of the configuration, the analysis can be restricted to the Representative Volume Element (RVE), as highlighted in Fig. 1c. Its geometry is described by two independent non-dimensional geometric parameters: the volume fraction of the teeth, ϕ_T, and the tooth tip angle, β_S, given by Li et al. (2013):

$$\phi_T = 1 - \frac{2\,h_L}{\lambda_S}, \qquad \tan\beta_S = \frac{\phi_T\,\lambda_S}{2\,A_S} = \frac{\lambda_S - 2h_L}{2\,A_S}, \tag{3}$$

with A_S and λ_S, respectively, the amplitude and wavelength of the suture, h_L the thickness of the interface layer measured in the $\boldsymbol{e}_1$ direction (Fig. 1c).

Regarding the constituents, i.e., the teeth and the interface layer, two simplifying hypothesis are made. The first is to consider the teeth and the interface layer perfectly bonded at the slant interfaces, the second is to assume the flat tip region unbonded. As discussed in Li et al. (2013), these assumptions do not affect the validity of the analysis. Both the teeth and the interface layer are also assumed homogeneous and their mechanical response is linear elastic, in the case of the teeth, and viscoelastic, in the case of the interface layer. The latter, in particular, is described by the Kelvin–Voigt model (Yu et al., 2020):

$$\begin{cases} \tau_L = G_L\,\gamma + \eta\,\dot{\gamma} & \text{shear behavior} \\ \sigma_L = E_L\,\varepsilon + \xi\,\dot{\varepsilon} & \text{normal behavior,} \end{cases} \tag{4}$$

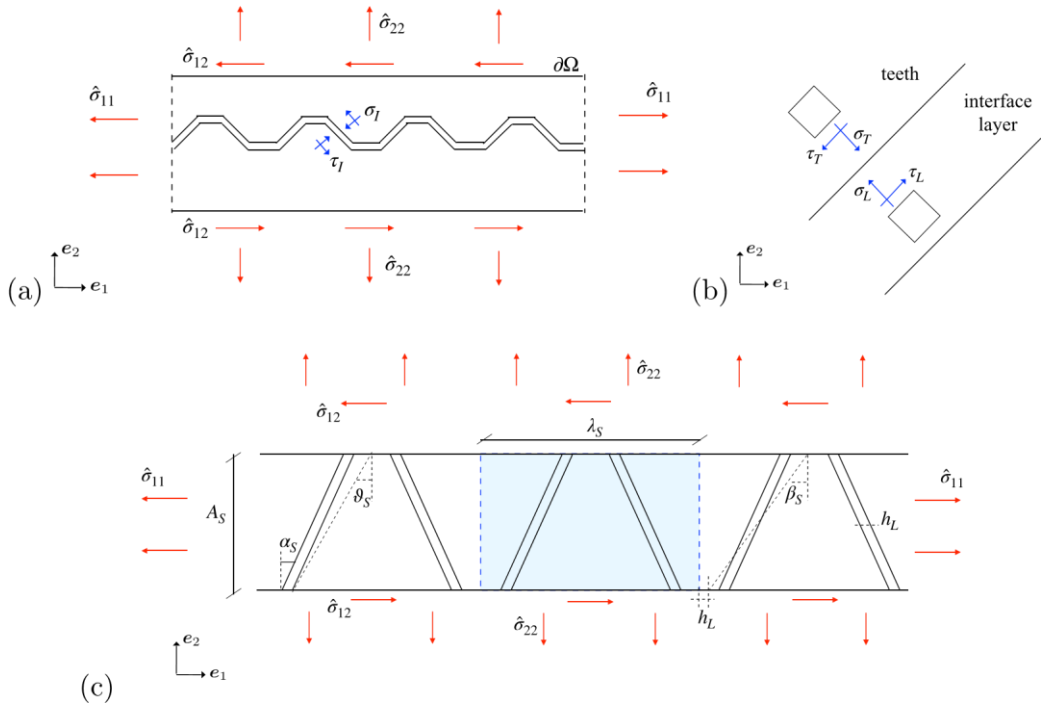

Fig. 1. (a) Schematic representation of a general trapezoidal suture joint indicating (b) the stresses acting at the interface and (c) the most relevant geometric parameters.

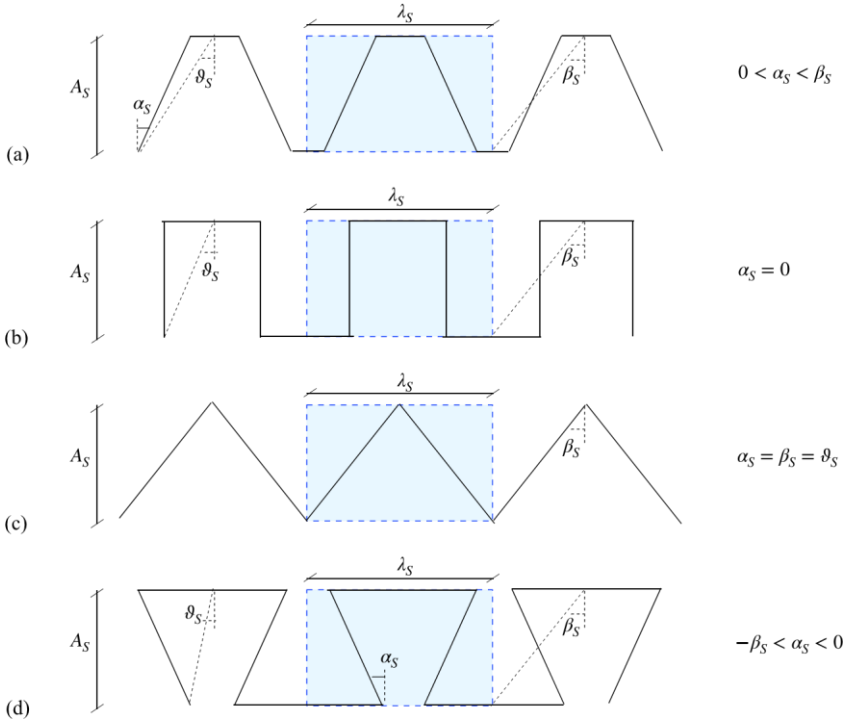

Fig. 2. Suture geometric profiles corresponding to different values of the angles α_S, β_S, ϑ_S: (a) trapezoidal, (b) rectangular, (c) triangular, (d) anti-trapezoidal.

with G_L and E_L, respectively, the layer shear modulus and Young's modulus, η the viscosity coefficient for shear deformation γ, ξ the viscosity coefficient for normal deformation ε and $(\dot{\cdot}) := \frac{d}{dt}(\cdot)$.

2.2. Effective properties

Closed-form relations for the effective in-plane Young's moduli, shear modulus and Poisson's ratios accounting the viscoelastic effect can be derived in the frequency domain by alternately prescribing a periodic loading condition

$$\hat{\boldsymbol{\sigma}}_1 = \begin{bmatrix} \hat{\sigma}_{11} \neq 0 \\ \hat{\sigma}_{22} = 0 \\ \hat{\sigma}_{12} = 0 \end{bmatrix}, \quad \hat{\boldsymbol{\sigma}}_2 = \begin{bmatrix} \hat{\sigma}_{11} = 0 \\ \hat{\sigma}_{22} \neq 0 \\ \hat{\sigma}_{12} = 0 \end{bmatrix}, \quad \hat{\boldsymbol{\sigma}}_3 = \begin{bmatrix} \hat{\sigma}_{11} = 0 \\ \hat{\sigma}_{22} = 0 \\ \hat{\sigma}_{12} \neq 0 \end{bmatrix} \tag{5}$$

described by

$\hat{\sigma}_{ij} = \Gamma_{ij} e^{i\omega t}, \qquad i, j = 1, 2,$ (6)

with Γ_{ij} the amplitude and ω the circular frequency of a time-harmonic plane wave propagating along the medium.

When dealing with viscoelastic materials, it is convenient to use the elastic–viscoelastic correspondence principle (Christensen, 2012), according to which the solution techniques developed for the linear elastic framework can be directly applied for viscoelastic media simply by replacing the elastic material parameters with their frequencydependent complex counterparts. A classical mechanics-based analysis (Li et al., 2013; Yu et al., 2020) can be thus applied, providing, in the loading condition $\hat{\sigma}_1$, the complex effective Young's modulus in the $\boldsymbol{e}_1$ direction

$$E_1 = \left(\frac{\lambda_S - 2h_L}{\lambda_S E_T} + \frac{2h_L}{\lambda_S} \left(\frac{\cos^2\alpha_S \sin^2\alpha_S}{\tilde{G}_L} + \frac{\cos^4\alpha_S}{E_L} \right) \right)^{-1} \equiv E_1' + iE_1''$$

and the related Poisson's ratio

$$\nu_{12} = -\left(\frac{E}{E} \right)_1 \left(2E_T + h_L \cos\alpha_S G_L + E_L \right)$$

(7)

$$\left(\frac{\lambda_S}{2A_S} \left(\frac{\nu_T A_S - \tilde{\nu}_L \frac{h_L}{E_L} \tan\beta_S}{\lambda_S} + h_L \cos\alpha_S \sin\alpha_S \left(\frac{\nu_T}{G_T} + \frac{\tilde{\nu}_L}{E_L} \right) \right) \right)$$

of the teeth, $G_L \equiv G_L + i\omega\eta$, $E_L \equiv E_L + i\omega\xi$ and $\tilde{\nu}_L$ the frequencywith E_T and ν_T, respectively, the Young's modulus and Poisson's ratio dependent shear modulus, Young's modulus and Poisson's ratio of the interface layer. According to the experimental observations in Pritz (2007), the frequency dependency of $\tilde{\nu}_L$ can be neglected and it is thus possible to assume $\tilde{\nu}_L \approx \nu_L$, being ν_L the constant, frequencyindependent elastic Poisson's ratio of the interface layer. Similarly, the loading state $\hat{\sigma}_2$ yields the complex effective Young's modulus in the $\boldsymbol{e}_2$ direction

$$E_2 = \frac{\lambda_S - 2h_L}{\lambda_S} \left(\frac{\psi}{E_T} + \frac{h_L \lambda_S - 2h_L}{2A_{2S}} \left(\frac{\cos^4\alpha_S}{G_L} + \frac{\cos^2\alpha_S \sin^2\alpha_S}{E_L} \right) \right)^{-1} \equiv E_2' + iE_2''$$

(8)

and the related Poisson's ratio

$$\nu_{21} = -\frac{\left(\frac{\nu_T}{E_T} - \frac{\tilde{\nu}_L}{E_L} \frac{h_L}{3} \right)\left(2h_L \right)\left(1 - \frac{1}{\lambda_S} \right) \Phi_1 - 1}{\psi \left(2A_S \left(r + \frac{\lambda_S - 2h_L}{E_T} \right) \lambda_S + 2h_L \Phi_1 \right)}$$

(9)

with

$$\begin{cases} 1 & \text{triangular} \\ 2/3 & \text{rectangular} \end{cases}$$

$$\left(2 - \frac{1}{\psi_{\alpha\beta}} \left(1 - \psi_{\alpha\beta} \right) \ln \left(\frac{1 + \psi_{\alpha\beta}}{1 - \psi_{\alpha\beta}} \right) \right) + \frac{1}{2\psi_{\alpha\beta 2}}$$

trapezoidal, anti-trapezoidal, (11)

$$\psi_{\alpha\beta} := \frac{\tan\alpha_S}{\tan\beta_S}$$

(12)

and

$$\Phi_1 := E_T \left(\frac{\cos^2\alpha}{3} + \frac{\sin^2\alpha}{5} + \frac{\cos^4\alpha}{E_L 5} \right)$$

$$\psi := \left(\frac{G_L}{(\quad)_2 (\quad)} \right)$$

(13)

Finally, the loading condition $\hat{\sigma}_3$ leads to the complex effective shear modulus

$$G_{12} = \left(\Phi_2 \left(\frac{\lambda_S - 2h_L \Phi_2}{4\Phi_3} 3 + \frac{5\Phi_3}{4E_T \tan^2\beta_S} \right) + \frac{\lambda_S \tan\alpha_S}{2A_S} \left(1 + \frac{2h_L}{\lambda_S \psi_{\alpha\beta}} \right) + \frac{3G_L}{2\Phi_3} \left(1 + \frac{3\Phi_3}{4E_T \tan^2\beta_S} \right) \right) \frac{1}{\lambda_S}$$

(14)

$$\equiv G_{12}' + iG_{12}'',$$

where, to simplify the notation,

$$\Phi_2 := G_L \tan^2\alpha_S + E_L, \qquad \Phi_3 := G_{\frac{\lambda_S - 2h_L}{T}} + 2G_L h_L,$$

(15)

and G_T the shear modulus of the teeth.

In Eqs. (7), (9), (14), $(\cdot)'$ and $(\cdot)''$ stand, respectively, for the storage and loss moduli of the suture joint, whose ratio defines the loss tangent

$$\equiv \frac{E''}{E'} \equiv \frac{G''}{G'}$$

$$\tan\delta_1 \equiv \frac{E_1''}{E_1'}, \quad \tan\delta_2 \equiv \frac{E_2''}{E_2'}, \tan\delta_{12} \equiv \frac{G_{12}''}{G_{12}'}$$

(16)

a useful parameter giving a measure of the ratio of the energy lost to the energy stored in a cyclic deformation (Ferry, 1980). This quantity allows us to evaluate the damping ability of the investigated system.

3. Discussion: the influence of the suture characteristics in the effective properties

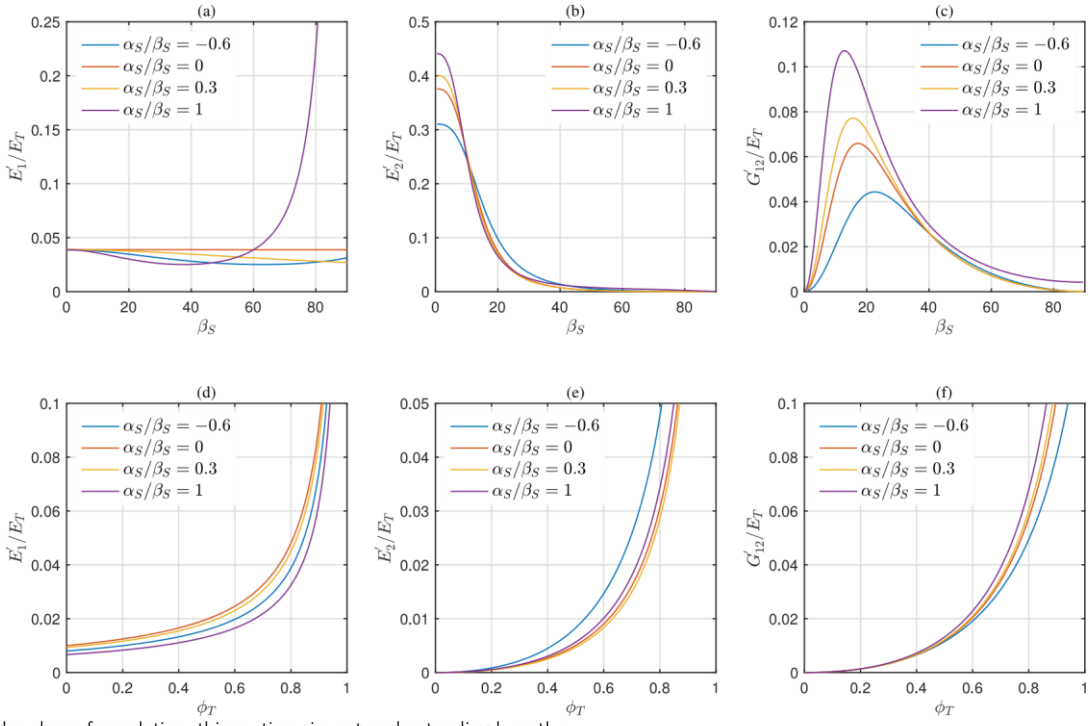

Fig. 3. The influence of the tooth tip angle β_S (first row) and teeth volume fraction ϕ_T (second row) in the normalised effective stiffness: (a), (d) Young's modulus E_1'/E_T; (b), (e) Young's modulus E_2'/E_T; (c), (f) shear modulus, G_{12}'/E_T.

According to the above formulation, this section aims at understanding how the suture geometric and mechanical parameters affect the effective properties. The analysis involves a suture joint having wavelength $\lambda_S = 15$ mm, amplitude $A_S = 15$ mm and where the teeth have Young's modulus $E_T = 6$ GPa, Poisson's ratio $\nu_T = 0.3$ and shear modulus $G_T = 2.3$ GPa. The interface layer has Young's modulus, $E_L = 10^{-2} E_T$, shear modulus $G_L = 10^{-2} G_T$, Poisson's ratio $\nu_L = 0.3$ and viscosity coefficients $\eta = \xi = 5$Pa · s. Four different configurations are investigated (Figs. 3–5), corresponding to different values of the ratio α_S/β_S: −0.6, −0.3, 0, 1 that provide a suture joint having, respectively, an anti-trapezoidal, trapezoidal, rectangular and triangular profile (Fig. 2).

In general, for a fixed value of the teeth volume fraction, $\phi_T = 0.75$, Figs. 3a, 3b, 3c suggest that increasing the tip angle β_S leads to an increase in the normalised Young's modulus E_1'/E_T, which is more significant for $\alpha_S/\beta_S = 1$, and to a decrease in the normalised Young's modulus E_2'/E_T. In terms of E_2'/E_T, the tooth tip angle has little influence for $\beta_S > 40^\circ$ while, for small values of β_S, E_2'/E_T increases very rapidly, especially in the case of the triangular profile (Fig. 3b).

A slightly different trend emerges in the case of the normalised shear modulus G_{12}'/E_T: an initial rapid increase for small values of β_S, followed by a peak region and a final decrease. However, as illustrated in Fig. 3c, to the triangular ($\alpha_S/\beta_S = 1$) and trapezoidal ($\alpha_S/\beta_S = 0.3$) profiles correspond an higher peak value of G_{12}'/E_T than that which occurs to the rectangular ($\alpha_S/\beta_S = 0$) and antitrapezoidal ($\alpha_S/\beta_S = -0.6$) ones. Fig. 3c also suggests that changing the value of α_S/β_S provides a shear stiffness G_{12}'/E_T reaching the peak value at different β_S. For example, varying α_S/β_S from 1 to 0.3 results in G_{12}'/E_T exhibiting a peak value, respectively, at $\beta_S \approx 11^\circ$ and $\beta_S \approx 15^\circ$. Regarding the effective Poisson's ratios ν_{12} and ν_{21}, it emerges a 'Poisson's switch' from positive to negative values, obtained by varying the angle β_S (Figs. 4a, 4b). However, the value of β_S at which the 'Poisson's switch' occurs is affected by α_S/β_S. For make it more clear, let us focus on Fig. 4a and let us consider the curves for $\alpha_S/\beta_S = -0.6$ and $\alpha_S/\beta_S = 0.3$ leading, respectively, to the antitrapezoidal and trapezoidal profiles. In the first case, the 'Poisson's switch' occurs at $\beta_S = 20^\circ$ while, in the second, at $\beta_S \approx 47^\circ$. Similar considerations apply for ν_{21} (Fig. 4b), which experiences a 'switch' from positive to negative values at different β_S, depending on the suture geometry. These findings, in accordance with Gao et al. (2018a) and Li et al. (2013), reveal the possibility to obtain a large control in the mechanics of suture joints and, in particular, an auxetic behavior can

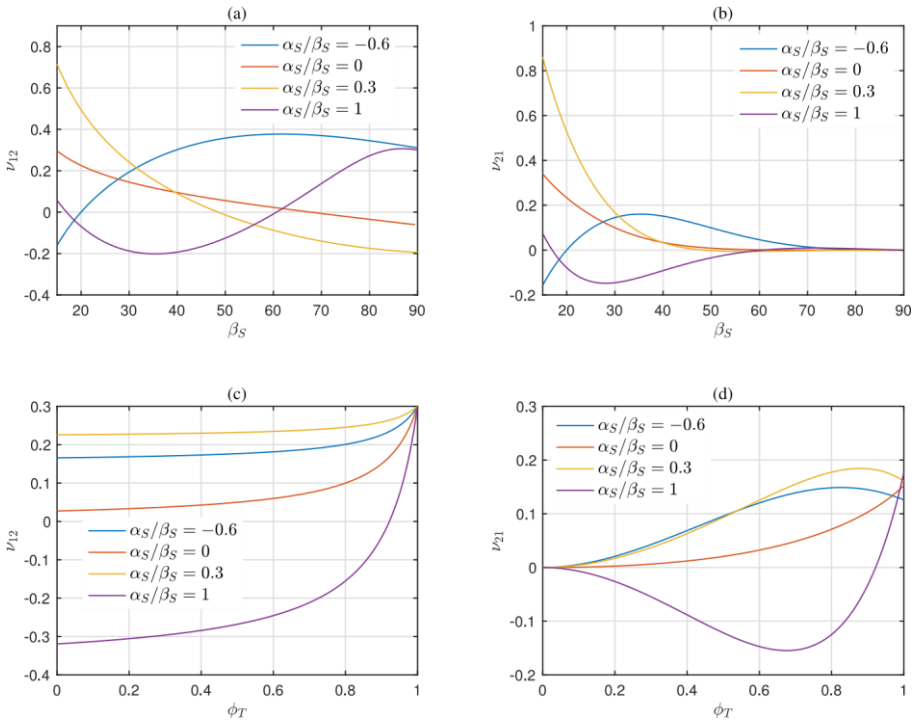

Fig. 4. The influence of the tooth tip angle β_S(first row) and teeth volume fraction ϕ_T(second row) in the effective Poisson's ratios: (a), (c) ν_{12}; (b), (d) ν_{21}.

be obtained simply by tailoring the geometric characteristics of the two Analogous considerations can be derived by focusing on the loss tanconstituents. gent tan δ_1, tan δ_2 and tan δ_{12} illustrated in Figs. 5a, 5b, 5c.

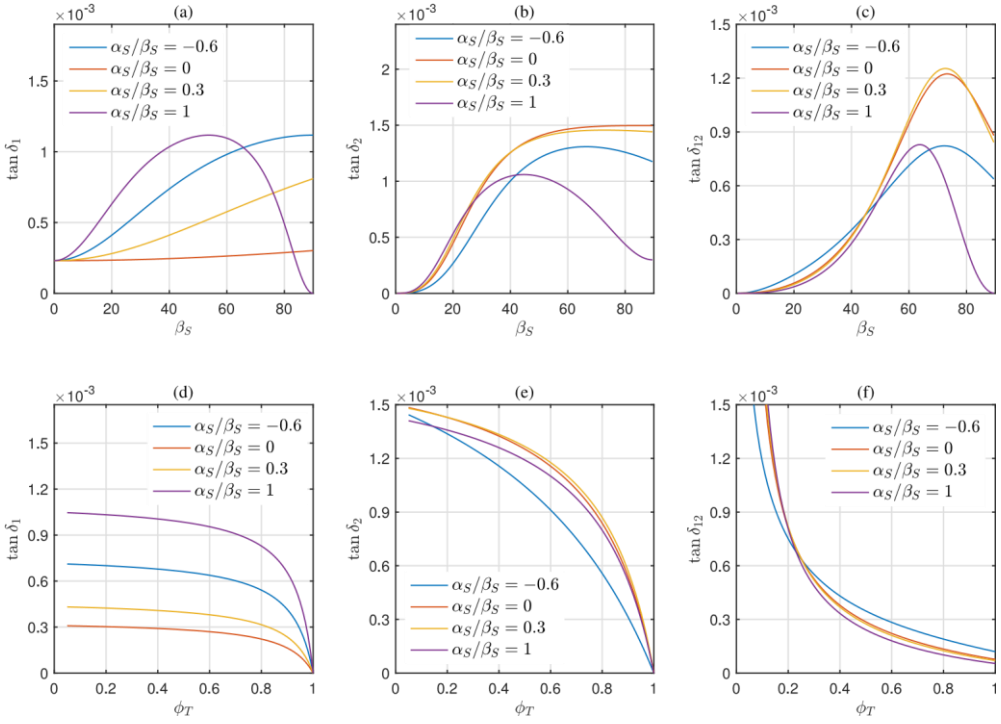

Fig. 5. The influence of the tooth tip angle β_S(first row) and teeth volume fraction ϕ_T(second row) in the loss tangent: (a), (d) tanδ_1; (b), (e) tanδ_2; (c), (f) tanδ_{12}.

Independently of the ratio α_S/β_S, the loss tangent appears to be strongly affected by the tooth tip angle $\beta_S$and, even a small increase of β_S, leads to an high increase in tan δ_1, tan δ_2 and tan δ_{12}.

Finally, regarding the influence of the teeth volume fraction ϕ_T, Figs. 3d, 3e, 3f reveal that, for a fixed value of the tooth tip angle $\beta_S = 30^\circ$, increasing ϕ_T leads to an increase of E_1'/E_T, E_2'/E_T and G_{12}'/E_T, regardless the geometric features of the suture profile. A common feature of

Figs. 5d, 5e, 5f is the higher dissipation achieved for small values of ϕ_T. This result can be explained by the fact that the lower ϕ_T, the higher will be the percentage of the viscoelastic interface layer, which is the element that dissipates energy rate.

4. Hierarchical extension

4.1. Overview

Let us imagine to modify the viscoelastic suture joint analysed in Section 2 by replacing the homogeneous interface layer with a structural element having the same periodic configuration of the starting system, i.e., two interdigitating stiff phases joined by a compliant interface layer. This modification can be iterated at successively smaller length scales, creating ever-finer structural detail while preserving the structure overall geometry. The resulting system, which will be referred to as viscoelastic hierarchical suture joint, is illustrated in Fig. 6, representing the general case of a level-[n] hierarchical suture joint, where n, the hierarchical order, is defined as the number of levels of scale displaying a recognised structure (Lakes, 1993).

For each level of hierarchy i, two sets of parameters define the configuration:

$$\Gamma_{[i-1]} := \left(A_{S[i-1]},\ \lambda_{S[i-1]},\ \alpha_{S[i-1]},\ \beta_{S[i-1]},\ \vartheta_{S[i-1]},\ h_{L[i-1]},\ G_{L[i-1]},\ E_{L[i-1]},\ \tilde{\nu}_{L[i-1]},\ G_{T[i-1]},\ E_{T[i-1]},\ \nu_{T[i-1]} \right),$$

$$\Gamma_{[i]} := \left(A_{S[i]},\ \lambda_{S[i]},\ \alpha_{S[i]},\ \beta_{S[i]},\ \vartheta_{S[i]},\ h_{L[i]},\ G_{L[i]},\ E_{L[i]},\ \tilde{\nu}_{L[i]},\ G_{T[i]},\ E_{T[i]},\ \nu_{T[i]} \right),$$

$$i=1,2,\ldots,n. \tag{17}$$

The first, $\Gamma_{[i-1]}$, describes the geometric ($A_{S[i-1]}$, $\lambda_{S[i-1]}$, $\alpha_{S[i-1]}$, $\beta_{S[i-1]}$, $\vartheta_{S[i-1]}$, $h_{L[i-1]}$) and mechanical ($G_{L[i-1]}$, $E_{L[i-1]}$, $\tilde{\nu}_{L[i-1]}$, $G_{T[i-1]}$, $E_{T[i-1]}$, $\nu_{T[i-1]}$) properties of the interface layer microstructure, the level-[$i-1$]. The second, $\Gamma_{[i]}$, defines the geometric ($A_{S[i]}$, $\lambda_{S[i]}$, $\alpha_{S[i]}$, $\beta_{S[i]}$, $\vartheta_{S[i]}$, $h_{L[i]}$) and mechanical ($G_{L[i]}$, $E_{L[i]}$, $\tilde{\nu}_{L[i]}$, $G_{T[i]}$, $E_{T[i]}$, $\nu_{T[i]}$) properties of the underlying large architecture, the level-[i].

By assuming that the size of its microstructure is fine enough to be negligible with respect to the level-[i] structure (Lakes, 1993), the interface layer can be treated as a continuum with effective properties having the same form of Eqs. (7)–(15). Consequently, for a level[i] hierarchical suture joint, the effective moduli can be evaluated in the frequency domain by adopting the same approach described in Section 2. Namely, by alternately applying the three loading situations in Eq. (5) and by solving the resulting mechanical problem by means of the elastic–viscoelastic correspondence principle in conjunction with the classical mechanics-based analysis presented in Li et al. (2013) and Yu et al. (2020).

4.2. Effective moduli

Let us focus on the level-[2] suture joint in Fig. 6 and, in particular, on the interface layer, the level-[1] structure. As it can be seen, it coincides with the suture joint analysed in Section 2 so that its effective Young's moduli, $E_1^{[1]}$ and $E_2^{[1]}$, shear modulus, $G_{12}^{[1]}$, and Poisson's ratios, $\nu_{12}^{[1]}$ and $\nu_{21}^{[1]}$, can be derived from Eqs. (7)–(15) by substituting A_S, λ_S, α_S, β_S, ϑ_S, h_L with $A_{S[1]}$, $\lambda_{S[1]}$, $\alpha_{S[1]}$, $\beta_{S[1]}$, $\vartheta_{S[1]}$, $h_{L[1]}$ and G_T, E_T, ν_T, G_L, E_L, $\tilde{\nu}_L$ with the parameters $G_{T[1]}$, $E_{T[1]}$, $\nu_{T[1]}$, $G_{L[1]}$, $E_{L[1]}$, $\tilde{\nu}_{L[1]}$, which specify the geometric and mechanical characteristics of the teeth and of the interface layer in the level-[1] suture joint. Note that, in the starting configuration, i.e., the level-[1], the interface layer does not have a microstructure, so that $G_L^{[1]} \equiv G_L$, $E_L^{[1]} \equiv E_L$, $\tilde{\nu}_L^{[1]} \equiv \tilde{\nu}_L$.

Having assumed that, at each hierarchical level, the length of scale of the sub-structure is fine enough to be negligible with respect to the super-structure (see Section 4.1), allows us to use $E_1^{[1]}$, $E_2^{[1]}$, $\nu_{12}^{[1]}$, $\nu_{21}^{[1]}$ and $G_{12}^{[1]}$ to obtain the effective moduli of the level-[2] suture joint. This

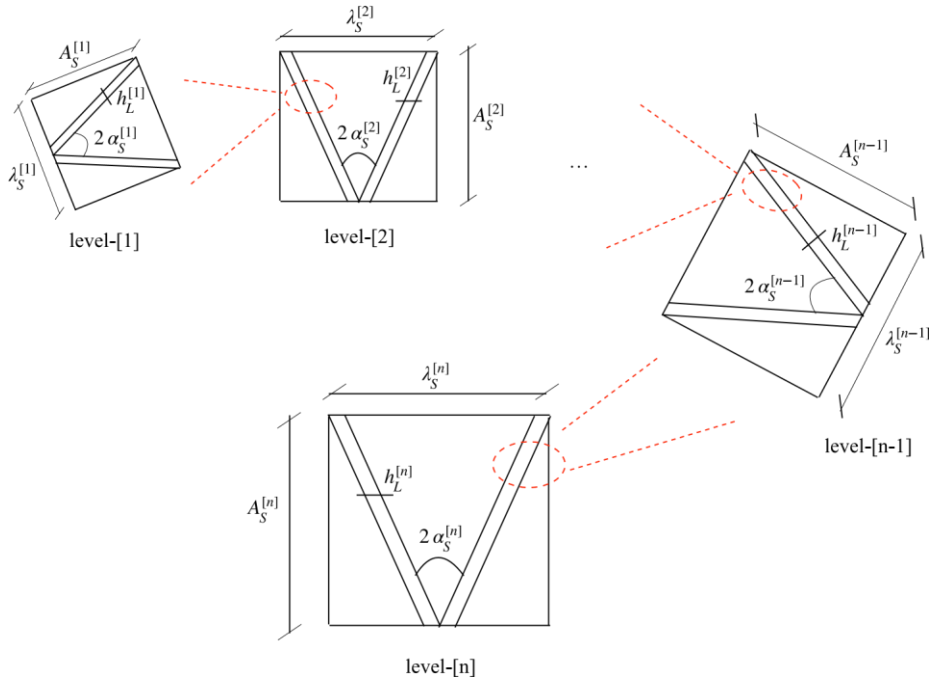

Fig. 6. Viscoelastic hierarchical suture joint: schematic representation and principal geometric parameters in the case of a self-similar triangular configuration.

can be done by

$$\frac{1}{E_T} + \frac{1}{E_L^{[n]}}\left(\frac{\lambda_S^{[n]}}{h_L^{[n]}}\frac{\cos\alpha_S}{\sin\alpha_S}\frac{A_S^{[n]}}{\lambda_S^{[n]}} - \frac{h_L^{[n]}}{\lambda_S^{[n]}}\right)\cos^2\alpha_S^{[n]} + \frac{1}{G_L^{[n]}}\left(1+\frac{h_L^{[n]}}{\lambda_S^{[n]}}\right)\sin^2\alpha_S^{[n]} - \frac{1}{E_1^{[n]}} = 0$$

replacing the geometric parameters A_S, λ_S, α_S, β_S, ϑ_S, h_L in Eqs. (7)–(15) with $A_{[2]S}$, $\lambda_{[2]S}$, $\alpha_{S[2]}$, $\beta_{S[2]}$, $\vartheta_{[2]S}$, $h_{[2]L}$ and G_T, E_T, ν_T, G_L, E_L, $\tilde{\nu}_L$ with $G_{T[2]}$, $E_{T[2]}$, $\nu_{T[2]}$, $G_{L[2]} \equiv G_{12[1]}$, $E_L^{[2]} \equiv E_1^{[1]}$, $\tilde{\nu}_L^{[2]} \equiv \nu_{12}^{[1]}$. Note that in the level-[2] suture joint and, in general, in suture joints with hierarchical order $i > 1$, the interface layer is not isotropic and in approximating it with an equivalent continuum, the effective properties in the longitudinal direction $\boldsymbol{e}_1$ have been considered (Sun et al., 2015; Gibson and Ashby, 1997).

Analogous considerations lead to effective moduli of the level-[n] hierarchical suture joint, derived from Eqs. (7)–(15) by substituting A_S, λ_S, α_S, β_S, ϑ_S, h_L with $A_{S[n]}$, $\lambda_{[S]n}$, $\alpha_{S[n]}$, $\beta_{S[n]}$, $\vartheta_{[S]n}$, $h_{[L]n}$ and G_T, E_T, ν_T, G_L, E_L, $\tilde{\nu}_L$ with $G_{T[n]}$, $E_{T[n]}$, $\nu_{T[n]}$, $G_{L[n]} \equiv G_{12[n]}$, $E_{L[n]} \equiv E_{1[n-1]}$, $\tilde{\nu}_{L[n]} \equiv \nu_{12[n-1]}$. It emerges that the effective Young's modulus and related Poisson's ratio in the $\boldsymbol{e}_1$ direction are given, respectively, by

$$E_1^{[n]} = \left(\frac{\lambda_{[S]n}^{[n]} - 2h_{[L]n}^{[n]}}{\lambda_S^{[n]}}\frac{1}{E_T^{[n]}} + \frac{2h_{[L]n}^{[n]}}{\lambda_S^{[n]}}\frac{\cos^2\alpha_{S[n]}^{[n]}\sin^2\alpha_{S[n]}^{[n]}}{G_{L[n]}^{[n]}} + \frac{\cos^4\alpha_{S[n]}^{[n]}}{\tilde{E}_{L[n]}^{[n]}}\right)^{-1}, \tag{18}$$

$$\nu_{12}^{[n]} = -\frac{\lambda_S^{[n]}}{2A_S^{[n]}}\left(\frac{-\frac{\nu_T^{[n]}}{E_T^{[n]}}A_S^{[n]} - \frac{\nu_L^{[n]}}{E_L^{[n]}}\frac{h_L^{[n]}}{\tan\beta_S^{[n]}} + h_L^{[n]}\cos^3\alpha_S^{[n]}\sin\alpha_S^{[n]}\left(\frac{1}{G_L^{[n]}} + \frac{1}{E_L^{[n]}}\right)}{\frac{\lambda_S^{[n]}}{2E_T^{[n]}} + h_L^{[n]}\cos^2\alpha_S^{[n]}\left(\frac{\sin^2\alpha_S^{[n]}}{G_L^{[n]}} + \frac{\cos^2\alpha_S^{[n]}}{E_L^{[n]}}\right)}\right), \tag{19}$$

while the corresponding quantities in the direction $\boldsymbol{e}_2$ take the form

$$E_2^{[n]} = \left(\frac{\lambda_{[S]n}^{[n]} - 2h_{[L]n}^{[n]}}{\lambda_S^{[n]}}\frac{\psi^{[n]}}{E_T^{[n]}} + \frac{h_{[L]n}^{[n]}\lambda_{S[n]}^{[n]} - 2h_{[L]n}^{[n]}}{2(A_{[S]n}^{[n]})^2}\frac{\cos^4\alpha_{S[n]}^{[n]}}{\tilde{G}_{L[n]}^{[n]}} + \frac{\cos^2\alpha_{S[n]}^{[n]}\sin^2\alpha_{S[n]}^{[n]}}{\tilde{E}_{L[n]}^{[n]}}\right)^{-1}, \tag{20}$$

$$\nu_{21}^{[n]} = \left(\frac{\nu_{T[n]}^{[n]}A_{S[n]}^{[n]}}{2A_S^{[n]}E_T^{[n]}} + \left(1 - \frac{\tilde{\nu}_{L[n]}^{[n]}h_{L[n]}^{[n]}}{\lambda_S - 2h_L}\tan\beta_S^{[n]}\right)\frac{\psi^{[n]}}{E_T^{[n]}}\right)\left(\lambda_S + 2h_L\right)\Phi_1^{[n]}, \tag{21}$$

with

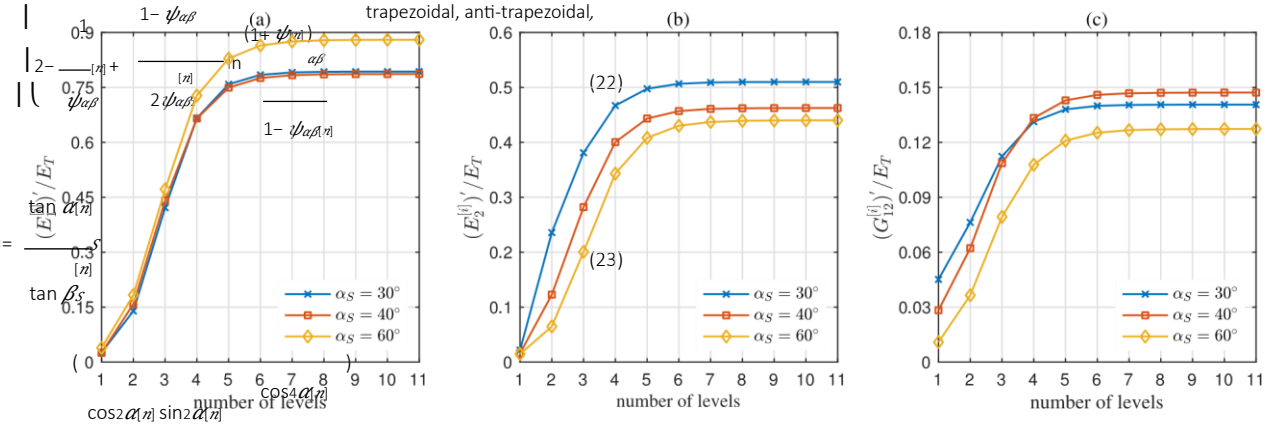

Fig. 7. Normalised effective stiffness of viscoelastic hierarchical suture joints vs number of levels : (a) $(E_1^{[i]})'/E_T$, (b) $(E_2^{[i]})'/E_T$, (c) $(G_{12}^{[i]})'/E_T$.

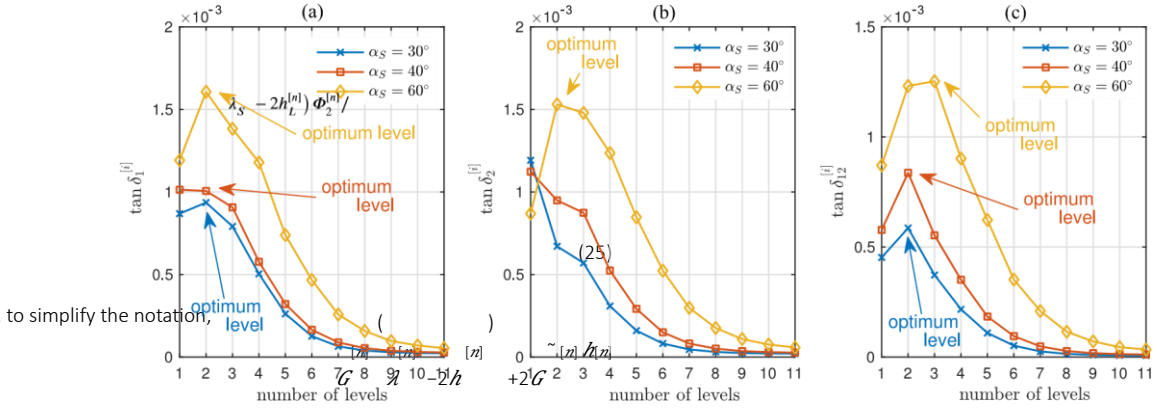

Fig. 8. Viscoelastic hierarchical suture joints: loss factors vs number of levels: (a) $\tan\delta_1^{[i]}$, (b) $\tan\delta_2^{[i]}$, (c) $\tan\delta_{12}^{[i]}$.

being, on order, $(\cdot)'$ and $(\cdot)''$ the storage and loss moduli of the level-$[n]$ hierarchical suture joint.

5. Parametric analysis and optimal values

From Eqs. (18)–(26) it clearly emerges that the effective moduli of a level-$[n]$ hierarchical suture joint are influenced not only by the geometric and mechanical properties of the two phases at level-$[n]$, but also by the corresponding characteristics of the smaller length scales. Motivated by the findings in Section 3, where even an auxetic behavior can be achieved for particular values of the tooth tip angle, this section aims at understanding how the suture characteristics affect the effective moduli in the case of structural hierarchy. The analysis deals with a viscoelastic hierarchical suture joint having up to 11 levels of hierarchy and, considering its abundant presence in biology, a self-similar triangular configuration with a constant value of teeth volume fraction at all levels. A self-similar entity, in particular, exhibits a statistically similar characteristic if examined both locally, at the level of individual components, and globally, at the level of the whole system (Chen and Pugno, 2013). It can be thus said that the same general trait is independent of the scale at which the observation is made (Katz, 1999) and this assumption renders the problem more treatable.

The starting element of the hierarchical arrangement considered, i.e., the level-[1] structure, has the same characteristics of the suture joint analysed in Section 3. Namely, wavelength λ_S= 15 mm, amplitude A_S= 15 mm, mechanical properties of the teeth given by E_T = 6 GPa, G_T = 2.3 GPa, ν_T = 0.3, and mechanical properties of the interface layer provided by $E_L = 10^{-2}E_T$, $G_L = 10^{-2}G_T$, ν_L = 0.3 and $\eta = \xi$ = 5Pa · s. Finally, a teeth volume fraction of ϕ_T = 0.75 is selected, value that is constant at all levels.

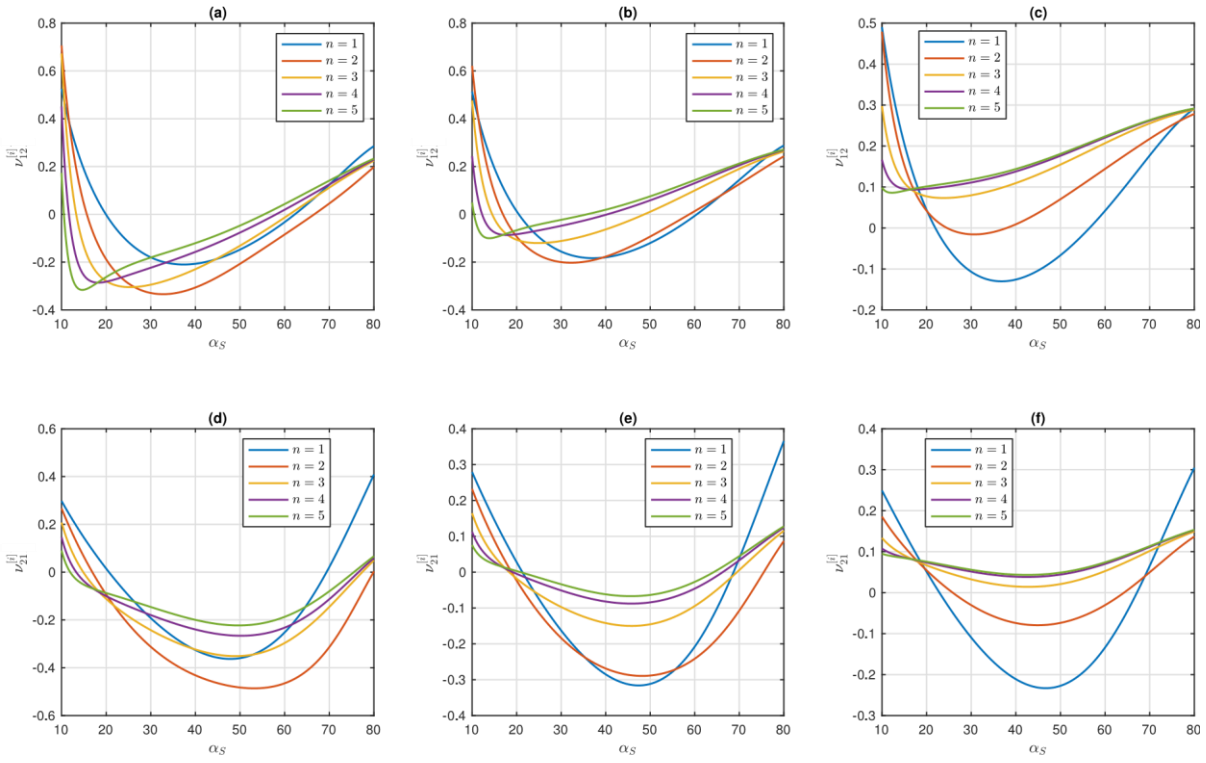

Fig. 9. The influence of the tooth tip angle α_S into the effective Poisson's ratios $\nu_{12}^{[\lambda]}$ (first row) and $\nu_{21}^{[\lambda]}$ (second row) in the case of (a), (d) $\phi_T = 0.6$; (b), (e) $\phi_T = 0.7$; (c), (f) $\phi_T = 0.8$.

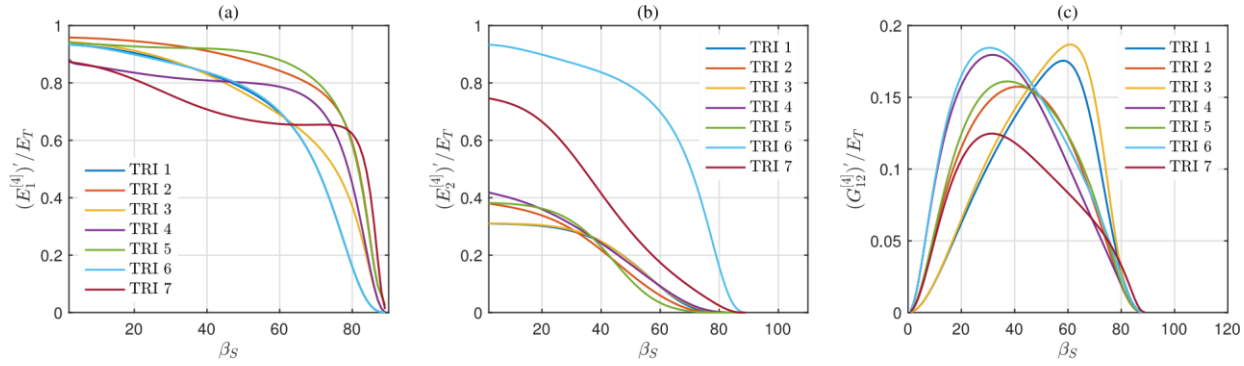

Fig. 10. Influence of the tooth tip angle β_S into the effective stiffness of hierarchical sutures having a triangular profile at the first level: (a) $(E_1^{[4]})'/E_T$, (b) $(E_2^{[4]})'/E_T$, (c) $(G_{12}^{[4]})'/E_T$.

Results are summarised in Figs. 7, 8, where the normalised effective stiffness $(E_1^{[i]})'/E_T$, $(E_2^{[i]})'/E_T$, $(G_{12}^{[i]})'/E_T$ and loss tangent tan $\delta_1^{[\lambda]}$, tan $\delta_2^{[\lambda]}$, tan $\delta_{12}^{[\lambda]}$ are plotted versus the number of levels, and in Fig. 9, where the effective Poisson's ratios $\nu_{12}^{[\lambda]}$, $\nu_{21}^{[\lambda]}$ are plotted versus the tooth tip angle $\alpha_S = \beta_S$. Note that, according to the assumption of self-similarity, α_S is constant at all levels.

As illustrated in Fig. 7, increasing the number of hierarchical levels leads to an increase in the effective stiffness, which is more significant≥ up to a number of orders $n < 5$. Conversely, when n 5, the curves reach a sort of plateau zone and increasing the number of levels provides a very small increase, independently of the value of the tooth tip angle α_S.

A different trend can be observed in Fig. 8 where, in the case of the loss tangent, increasing the number of hierarchical levels leads to a significant improvement only for particular values of the parameter α_S. For example, if we focus on tan $\delta_2^{[\lambda]}$ it emerges that hierarchy is detrimental for $\alpha_S = 30^\circ$, 40° while, for $\alpha_S = 60^\circ$, adding hierarchy leads to an improvement up to the second level, which coincides with the optimum level of this particular configuration (Fig. 8b).

Regarding the Poisson's ratios in Fig. 9, only the curves corresponding to the first 5 levels of hierarchy are considered, allowing us to provide a more clear representation. Also, to deeply investigate the possibility to obtain auxeticity in the hierarchical context, three different values of teeth volume fraction are examined: $\phi_T = 0.6$, 0.7, 0.8. Generally, an auxetic response appears for all the investigated cases, even if a large variability in the values of $\nu_{12}^{[\lambda]}$ and $\nu_{21}^{[\lambda]}$ can be obtained simply by modifying the angle α_S and the number of hierarchical levels n. This aspect is well illustrated in Figs. 9c, 9f where, for $\phi_T = 0.8$, auxeticity emerges only for $n = 1$, 2 while, when $n = 3$, 4, 5, the effective Poisson's ratios are always positive. Conversely, $\phi_T = 0.6$ (Figs. 9a, 9d) and $\phi_T = 0.7$ (Figs. 9b, 9e), lead to an auxetic response independently of the hierarchical order considered. By comparing Figs. 9a, 9d and Figs. 9b, 9e, we also observe that increasing the teeth volume fraction from $\phi_T = 0.6$ to $\phi_T = 0.7$ reduces the minimum value of $\nu_{12}^{[\lambda]}$ and $\nu_{21}^{[\lambda]}$ that can be achieved.

From these results, it can be said that there exist a synergy of hierarchy, geometric features and material heterogeneity in obtaining auxeticity.

6. Different levels with different geometry

To further investigate how the suture parameters can be optimised to improve its mechanical response in the hierarchical context, this section deals with a four-level viscoelastic hierarchical suture joint having different waveforms at each level: triangular, rectangular, trapezoidal and anti-trapezoidal. Such geometries are obtained, respectively, for $\alpha_S/\beta_S = 1$, $\alpha_S/\beta_S = 0$, $\alpha_S/\beta_S = 0.6$ and $\alpha_S/\beta_S = -0.6$ (Fig. 1).

In all the examined configurations (Table 1), the starting element, i.e., the level-[1], has teeth with Young's modulus $E_T = 6$ GPa, shear modulus $G_T = 2.3$ GPa, Poisson's ratio $\nu_T = 0.3$ and viscoelastic interface layer with Young's modulus $E_L = 10^{-1}E_T$, shear modulus $G_L = 10^{-1}G_T$, Poisson's ratio $\nu_L = 0.3$ and viscosity coefficients $\eta = \xi = 50\text{Pa}\cdot\text{s}$. Also, a teeth volume fraction of $\phi_T = 0.75$ is selected, value that is constant at all levels.

To keep the paper concise, results are reported for the first four configurations (TRI1, TRI2, TRI3, TRI4) only. For additional details, the interested reader is referred to the Supplementary Material. In terms of effective stiffness $(E_1^{[4]})'/E_T$, $(E_2^{[4]})'/E_T$ and $(G_{12}^{[4]})'/E_T$, we observe a decrease provided by increasing the tooth tip angle β_S(Fig. 10).

As expected, different results emerge from the examined configurations. For example, having a rectangular (TRI2, TRI5) profile at the fourth level yields higher values of $(E_1^{[4]})'/E_T$(Fig. 10a) while the arrangement in TRI6 experiences superior $(E_2^{[4]})'/E_T$(Fig. 10b).

Fig. 10c reveals the existence of a particular value of β_S, $\beta_S^* \approx 46^\circ$, such that

$$\left(\frac{(G_{12}^{[4]})'}{E_T}\right)_{\text{TRI6, TRI4}} > \left(\frac{(G_{12}^{[4]})'}{E_T}\right)_{\text{TRI1, TRI3}} \quad \text{for } \beta_S < \beta_S^*, \tag{28}$$

$$\left(\frac{(G_{12}^{[4]})'}{E_T}\right)_{\text{TRI6, TRI4}} < \left(\frac{(G_{12}^{[4]})'}{E_T}\right)_{\text{TRI1, TRI3}} \quad \text{for } \beta_S > \beta_S^*. \tag{29}$$

Table 1
Different levels with different geometry: hierarchical configurations examined.

	Level-[1]	Level-[2]	Level-[3]	Level-[4]
TRI1	triangular	trapezoidal	rectangular	anti-trapezoidal
TRI2	triangular	trapezoidal	anti-trapezoidal	rectangular
TRI3	triangular	rectangular	trapezoidal	anti-trapezoidal
TRI4	triangular	rectangular	anti-trapezoidal	trapezoidal
TRI5	triangular	anti-trapezoidal	trapezoidal	rectangular
TRI6	triangular	anti-trapezoidal	rectangular	trapezoidal
TRI7	triangular	triangular	triangular	triangular
TRA1	trapezoidal	triangular	rectangular	anti-trapezoidal
TRA2	trapezoidal	triangular	anti-trapezoidal	rectangular
TRA3	trapezoidal	rectangular	triangular	anti-trapezoidal
TRA4	trapezoidal	rectangular	anti-trapezoidal	triangular
TRA5	trapezoidal	anti-trapezoidal	triangular	rectangular
TRA6	trapezoidal	anti-trapezoidal	rectangular	triangular
TRA7	trapezoidal	trapezoidal	trapezoidal	trapezoidal
REC1	rectangular	triangular	trapezoidal	anti-trapezoidal
REC2	rectangular	triangular	anti-trapezoidal	trapezoidal
REC3	rectangular	trapezoidal	triangular	anti-trapezoidal
REC4	rectangular	trapezoidal	anti-trapezoidal	triangular
REC5	rectangular	anti-trapezoidal	triangular	trapezoidal
REC6	rectangular	anti-trapezoidal	trapezoidal	triangular
REC7	rectangular	rectangular	rectangular	rectangular
ANTI1	anti-trapezoidal	triangular	trapezoidal	rectangular
ANTI2	anti-trapezoidal	triangular	rectangular	trapezoidal
ANTI3	anti-trapezoidal	trapezoidal	triangular	rectangular
ANTI4	anti-trapezoidal	trapezoidal	rectangular	triangular
ANTI5	anti-trapezoidal	rectangular	triangular	trapezoidal
ANTI6	anti-trapezoidal	rectangular	trapezoidal	triangular
ANTI7	anti-trapezoidal	anti-trapezoidal	anti-trapezoidal	anti-trapezoidal

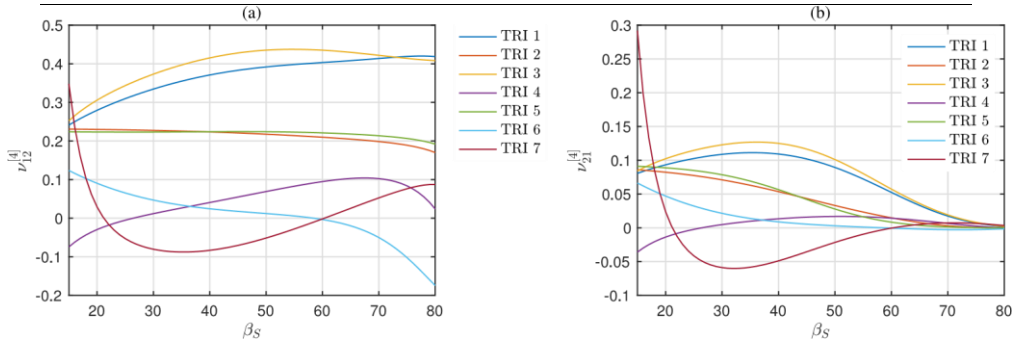

Fig. 11. Influence of the tooth tip angle β_S into the effective Poisson's ratios of hierarchical sutures having a triangular profile at the first level: (a) $\nu_{12}^{[4]}$, (b) $\nu_{21}^{[4]}$.

That is to say, for small values of β_S, $\beta_S < \beta_S^*$, the hierarchical arrangements TRI6, TRI4 (with a trapezoidal geometry at the fourth level) are stiffer than TRI1, TRI3 (with an anti-trapezoidal profile at the fourth level) while, for $\beta_S > \beta_S^*$, an opposite trend appears.

Figs. 11 suggests that the suture profile at different levels is an important parameter to achieve an auxetic response. For example, if we consider Fig. 11a, we observe that auxeticity can be obtained only with a triangular (TRI7) or trapezoidal (TRI5, TRI4) geometry at level-[4].

A common feature of Fig. 12 is that, in all the examined configurations, for the loss tangent $\tan\delta_1^{[4]}$, $\tan\delta_2^{[4]}$, $\tan\delta_{12}^{[4]}$ the effect of β_S is generally minimal for $\beta_S < 40^\circ$. However, different levels of dissipation are provided by the different configurations examined. For example, TRI7 (triangular profile at all levels) experiences higher values of $\tan\delta^{[4]}$ (Fig. 12a) while, in terms of $\tan\delta^{[4]}$, higher values are observed

$_1$ $_{12}$

for TRI1, TRI3 (with an anti-trapezoidal waveform at level-[4]).

In the context of hierarchical suture joints, these results reveal the possibility to improve the mechanical response, in terms of stiffness, auxeticity and dissipation levels, by adopting a sort of 'mix and match' approach. That is to say, an approach in which different levels have different geometric features.

7. An application of the theory to the sinusoidal patterned sutures in biology

As a real-case example, in this section we apply the theoretical concepts presented in Section 2 to obtain the effective stiffness of sinusoidal sutures, typical of many biological systems (Fig. 13). Examples include the red-bellied woodpecker beak (Lee et al., 2014) and the common millet seedcoat (Hasseldine et al., 2017), where the sinusoidal geometry has been demonstrated to be responsible for increasing energy dissipation and impact resistance, sea urchins, where the sinusoidal architecture has been developed to force cracks to follow a specific pattern, and the cranium of different biological species like monkeys (Wang et al., 2010), goats (Jaslow and Biewener, 1995),

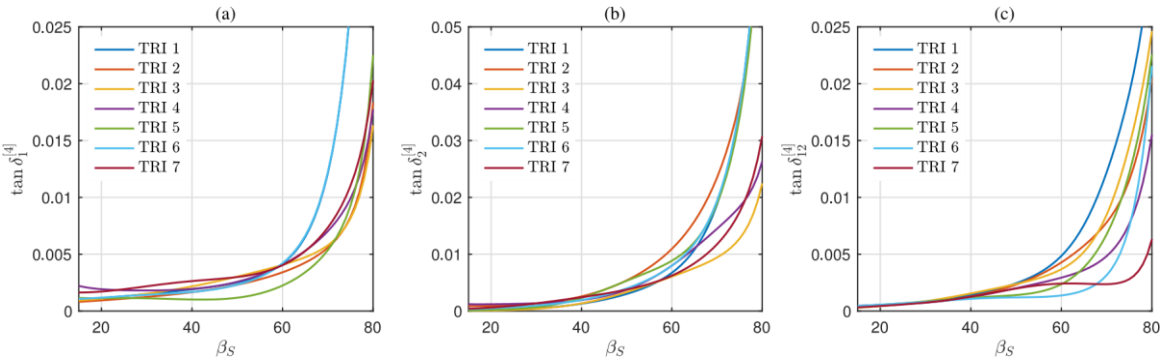

Fig. 12. Influence of the tooth tip angle β_S into the loss tangent of hierarchical sutures having a triangular profile at the first level: (a) $\tan\delta_1^{[4]}$, (b) $\tan\delta_2^{[4]}$ (c) $\tan\delta_{12}^{[4]}$.

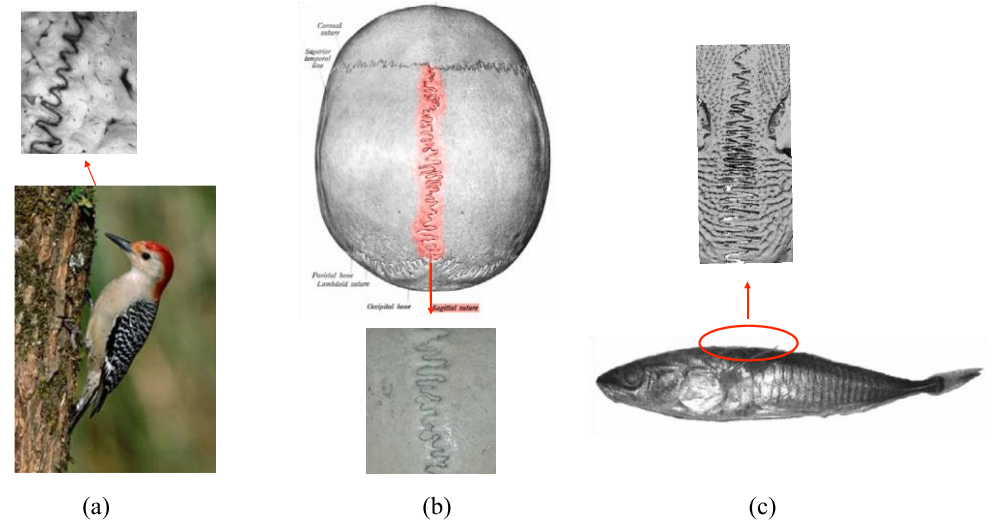

Fig. 13. Sinusoidal sutures in biology: (a) red-bellied woodpecker beak (modified from Lee et al. (2014) and https://houstonaudubon.org), (b) sagittal sutures of the human cranium (modified from https://shortnotesinplasticsurgery.wordpress.com, https://en.wikipedia.org/wiki/Sagittal_suture), (c) marine threespine stickleback (modified from Song et al., 2010).

lizards (Moazen et al., 2009), dinosaurs (Rayfield, 2004) and humans (Liu et al., 2017; Jaslow, 1990). Cranial sutures, in particular, provide the cranial bone flexibility for growth and movement, alleviate stress during mastication and impact phenomena, and greatly enhance the overall stiffness and strength (Jaslow, 1990).

Similarly to Section 2, in deriving the effective stiffness of the sinusoidal suture, our attention is focused on the interdigitating area and, due to the periodicity of the configuration, only the Representative Volume Element is considered (Fig. 14). From a geometrical point of view, its configuration is described by the two parameters ϕ_L, volume fraction of the teeth, and β_S, tooth tip angle, given respectively by Hasseldine et al. (2017)

$$\phi_T = 1 - \frac{\lambda_S\left(2A_S + h_L\right)}{\lambda_S}, \qquad \beta_S = \tan^{-1}\left(4\frac{A_S}{\lambda_S}\right), \tag{30}$$

with A_S and λ_S, in turn, the amplitude and wavelength of the suture, h_L the thickness of the interface layer,

$$s = \int_0^{\lambda_S} \sqrt{1 + \left(\frac{dy_S(x)}{dx}\right)^2}\, dx \tag{31}$$

the arc length of the sinusoidal wave profile (Hosseini et al., 2019)

$$y_S(x) = A_S\left[1 + \sin\left(2\pi\left(\frac{x}{\lambda_S} - \frac{1}{4}\right)\right)\right] \tag{32}$$

within one wavelength.

The simplifying hypothesis of Section 2, i.e., teeth and interface layer homogeneous and perfectly bonded at the interfaces, still apply.

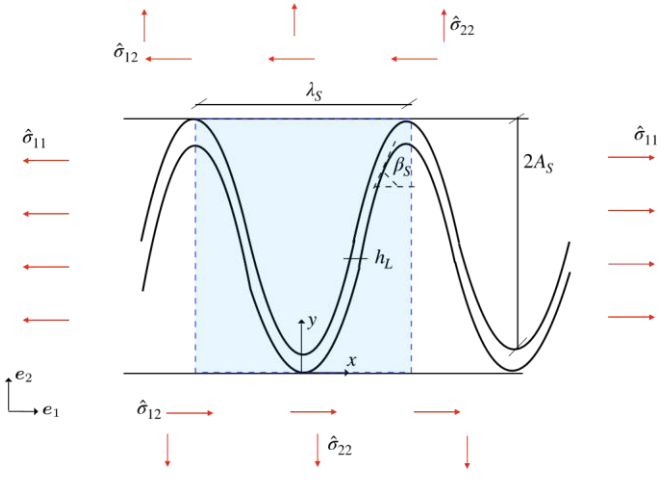

Fig. 14. Schematic representation of a sinusoidal suture joint indicating the most relevant geometric parameters.

Again, a linear elastic mechanical behavior is assumed for the teeth and a viscoelastic response described by the Kelvin–Voigt model is considered for the interface layer.

To derive the effective stiffness of the sinusoidal suture, the same methodology of Section 2 can be adopted. That is, by alternately prescribing the loading conditions in Eq. (5) and solving the corresponding problem by using the mechanics-based analysis of Li et al. (2013), Yu et al. (2020), together with the elastic–viscoelastic correspondence principle. In this example, for simplicity, only the effective Young's moduli in the $\boldsymbol{e}_1$ and $\boldsymbol{e}_2$ direction are considered. They are given, respectively, by

$$E_1^* = \left[\left(1-\phi_T\right)\left(\frac{\cos^2\beta_S \sin^2\beta_S}{G_L^*} + \frac{\cos^4\beta_S}{E_L^*}\right) + \frac{\phi_T}{E_T}\right]^{-1} \equiv E_1' + iE_1'' \quad (33)$$

and

$$E_2^* = \left[\frac{\phi_T}{E_T} + \left(1-\phi_T\right)\left(\frac{\cos^2\beta_S \sin^2\beta_S}{G_L^*} + \frac{\sin^4\beta_S}{E_L^*}\right)\right]^{-1} \equiv E_2' + iE_2'', \quad (34)$$

with E_T the Young's modulus of the teeth, $\tilde{G}_L$ and $\tilde{E}_L$ the frequency-dependent shear modulus and Young's modulus of the interface layer (cf. Section 2.2), $(\cdot)'$ and $(\cdot)''$, respectively, the storage and loss moduli of the suture, such that their ratio provides the loss tangent $\tan\delta_1 \equiv E_1''/E_1'$ and $\tan\delta_2 \equiv E_2''/E_2'$.

From Eqs. (33),(34) it clearly emerges that the effective moduli of a sinusoidal suture are strongly affected by the suture waviness $\chi := 2A_S/\lambda_S$, i.e., the ratio between the suture height and the suture wavelength, via the parameter β_S. In biology, the values of χ vary between 1, in the case of the woodpecker beak (Lee et al., 2014), and approximately 4 in the case of the cranium (Liu et al., 2017). This leads to higher values of effective stiffness, as illustrated in Fig. 15, where E_1'/E_T and E_2'/E_T are plotted against the parameter χ. Fig. 15, in particular, is based on the data for the human cranium (Liu et al., 2017): tooth material with E_T = 6 GPa, ν_T = 0.3, G_T = 2.3 GPa; interface layer with E_L = 80 MPa, ν_L = 0.4, G_L = 26.8 MPa and h_L = 0.2 mm, providing ϕ_T = 0.85; A_S = 5.4 mm and λ_S = 2.7 mm leading to χ = 4 and $\beta_S \approx 7.1^\circ$. Finally, we have assumed $\eta = \xi$ = 5 Pa·s. From Fig. 15 it can be said that this particular configuration is the optimal one to obtain higher values of stiffness since an increase in χ, provided by fixing λ_S and varying A_S, does not produce significant additional benefits. Conversely, a decrease in the effective stiffness is observed by decreasing χ.

A different trend emerges for the loss tangent illustrated in Fig. 16. As it can be seen, to small values of χ, i.e., $\chi \lesssim 1.5$, correspond high values of tan δ_1 and tan δ_2 while a sort of plateau can be observed for $\chi \gtrsim 2.5$. As expected, a very high dissipation level is observed for $\chi = 1$, value that coincides with the waviness of the red-bellied woodpecker beak. It can be thus said that while the waviness of the cranium is optimised to obtain high stiffness, that of the woodpecker beak, due to its particular function, is optimised to obtain high levels of dissipation.

Even if a detailed analysis of the sinusoidal sutures in biology and, in particular, of the sinusoidal sutures of the cranium, goes beyond the aim of our work (more sophisticated techniques are required), these results confirm two important aspects. The first, is the great advantage offered by suture joints, the second is that biological systems are efficiently designed to obtain an optimal mechanical behavior.

8. Conclusions

This paper deals with the analysis of viscoelastic suture joints having a general trapezoidal waveform.

Firstly, based on the elastic–viscoelastic correspondence principle, a theoretical model leading to closed-form expressions for the effective properties (Young's moduli, shear modulus, Poisson's ratios) and loss factors is presented. A strong influence of the suture geometric and mechanical characteristics on the effective behavior emerges and the results of a parametric analysis to investigate this aspect are reported. By carefully tailoring the suture parameters, i.e., geometric profile, tooth tip angle and teeth volume fraction, not only an improvement in the effective stiffness and loss moduli, but also an auxetic response, can be obtained.

Viscoelastic hierarchical suture joints, obtained by adding some levels of hierarchy into the starting system, are also investigated. The application of the elastic–viscoelastic correspondence principle leads to explicit relations for the effective Young's modulus, shear modulus, Poisson's ratios and loss factors. These quantities are closely related to the suture characteristics at all levels and the example of a selfsimilar hierarchical structure with eleven orders of hierarchy clarify this. The analysis reveals that introducing hierarchy improves the effective moduli and loss factors of the non-hierarchical counterpart. Optimal levels of hierarchy can be identified and, similarly to the nonhierarchical case, auxeticity appears for certain values of the suture tooth tip angle and volume fraction. The example of a four-level viscoelastic suture joint having different waveforms at each level is then presented. This sort of 'mix and match' approach illustrates how the geometric characteristics of the suture at different levels are an

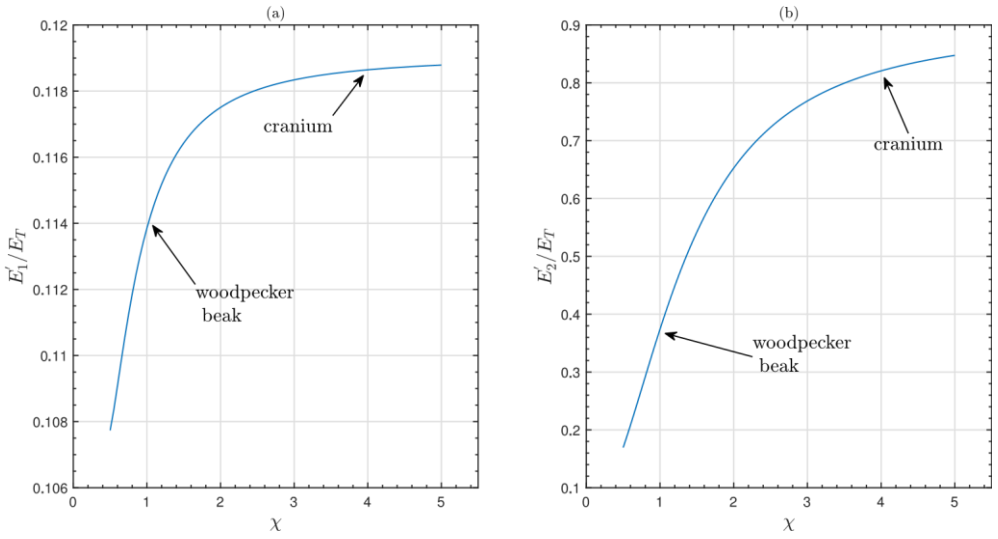

Fig. 15. An example from biology: the sinusoidal sutures of the cranium. Influence of the waviness χ in the normalised effective stiffness: (a) Young's modulus E_1'/E_T, (b) Young's modulus E_2'/E_T.

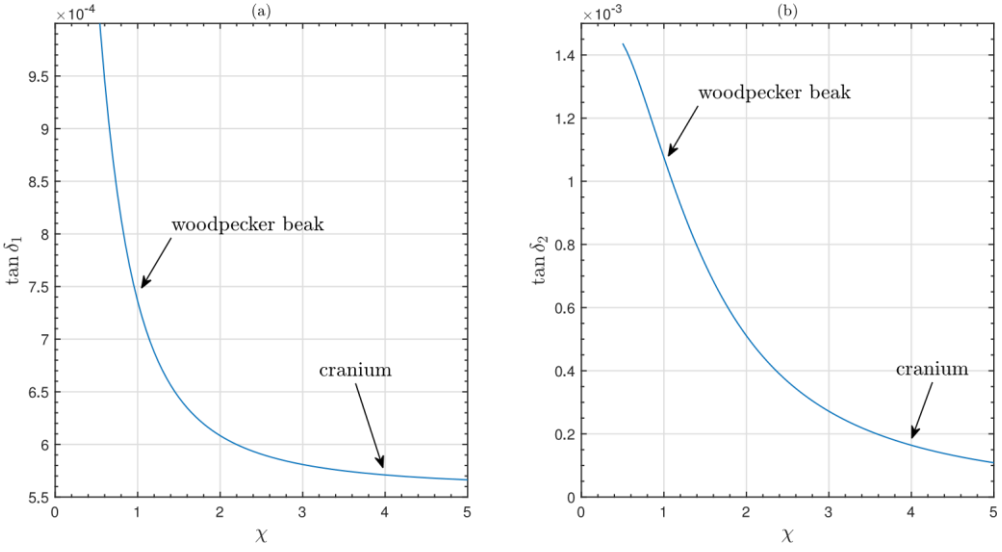

Fig. 16. The sinusoidal sutures of the cranium: influence of the waviness χ in the loss tangent (a) $\tan\delta_1$, (b) $\tan\delta_2$.

important parameter in terms of effective stiffness and dissipation level and suggests a possible design concept for bioinspired materials based on structural hierarchy, material mixing and geometric 'mix and match' approach. An extension of the theory to the sinusoidal patterned sutures in biology is also included. By considering the cranial sutures as a real-case example, the analysis confirms the functional significance of biological sutures, as well as the efficiency of biological systems in obtaining an optimal mechanical behavior. In particular, if compared to the sinusoidal sutures of the woodpecker beak, it emerges that the configuration of cranial sutures is optimised to obtain high stiffness, while that of the woodpecker beak for providing high energy dissipation levels. Compared to the previous works, this comprehensive study is the first to explore the mechanical behavior of suture joints with the consideration of both hierarchy and viscoelasticity.

Declaration of competing interest

The authors declare that they have no known competing financial interests or personal relationships that could have appeared to influence the work reported in this paper.

Data availability

Data will be made available on request

Acknowledgements

F. Ongaro and N. M. Pugno are supported by the EU H2020 FETOpen project Boheme, Grant agreement No. 863179.

References

Allen, E.G., 2007. Understanding ammonoid sutures: new insights into the dynamic evolution of paleozoic suture morphology. In: Cephalopods Present and Past: New Insights and Fresh Perspectives. pp. 159–180.

Cao, Y., Wang, W., Wang, J., Zhang, C., 2019. Experimental and numerical study on tensile failure behavior of bionic suture joints. J. Mech. Behav. Biomed. Mater. 92, 40–49.

Chen, Q., Pugno, N.M., 2013. Biomimetic mechanisms of natural hierarchical materials: a review. J. Mech. Behav. Biomed. Mater. 19, 3–33.

Chen, I.H., Yang, W., Meyers, M.A., 2015. Leatherback sea turtle shell: a tough and flexible biological design. Acta Biomater. 28, 2–12.

Christensen, R., 2012. Theory of Viscoelasticity: An Introduction. Elsevier.

Damiens, R., Rhee, H., Hwang, Y., Park, S.J., Hammi, Y., Lim, H., Horstemeyer, M.F., 2012. Compressive behavior of a turtle shell: experiment, modeling, and simulation. J. Mech. Behav. Biomed. Mater. 6, 106–112.

De Blasio, F.V., 2008. The role of suture complexity in diminishing strain and stress in ammonoid phragmocones. Lethaia 41, 15–24.

De Stefano, M., De Stefano, L., Congestri, R., 2009. Functional morphology of microand nanostructures in two distinct diatom frustules. Superlattices Microstruct. 46, 64–68.

Farr, R.S., 2007. Fractal design for an efficient shell strut under gentle compressive loading. Phys. Rev. E 76.

Ferry, J., 1980. Viscoelastic Properties of Polymers. John Wiley and Sons.

Gao, C., Hasseldine, B.P.J., Li, L., Weaver, J.C., Li, Y., 2018a. Amplifying strength, toughness, and auxeticity via wavy sutural tessellation in plant seedcoats. Adv. Mater.

Gao, C., Li, Y., 2019a. Mechanical model of bio-inspired composites with sutural tessellation. J. Mech. Phys. Solids 122, 190–204.

Gao, C., Slesarenko, V., Boyce, M.C., Rudykh, S., Li, Y., 2018b. Instability-induced pattern transformation in soft metamaterial with hexagonal networks for tunable wave propagation. Sci. Rep. 8.

Ghazlan, A., Ngo, T.D., Tran, P., 2015. Influence of interfacial geometry on the energy absorption capacity and load sharing mechanisms of nacreous com- posite shells. Comput. Struct. 132, 299–309.

Gibson, L.J., Ashby, M.F., 1997. Cellular Solids, Structures and Properties. Cambridge University Press.

Hartwig, W.C., 1991. Fractal analysis of sagittal suture morphology. J. Morphol. 210, 289–298.

Hasseldine, B.P.J, Gao, C., Collins, J.M., Jung, H.D., Jang, T.S., Song, J., 2017. Mechanical response of common millet (*Panicum miliaceum*) seeds under quasistatic compression: Experiments and modeling. J. Mech. Behav. Biomed. Mater. 73, 102–113.

Hosseini, M.S., Cordisco, F.A., Zavatteri, P.D., 2019. Analysis of bioinspired noninterlocking geometrically patterned interfaces under predominant mode I loading. J. Mech. Behav. Biomed. Mater. 96, 244–260.

Hubbard, R.P., Melvin, J.W., 1971. Flexure of cranial sutures. J. Biomech. 4, 491–496.

Jasinoski, S.C., Reddy, B.D., Louw, K.K., Chinsamy, A., 2010. Mechanics of cranial sutures using the finite element method. J. Biomech. 43, 3104–3111.

Jaslow, C.R., 1990. Mechanical properties of cranial sutures. J. Biomech. 23.

Jaslow, C.R., Biewener, A.A., 1995. Strain patterns in the horncores, cranial bones and sutures of goats (*Capra hircus*) during impact loading. J. Zool. 235.

Katz, J.S., 1999. The self-similar science system. Res. Policy 28, 501–517.

Krauss, S., Monsonego-Ornan, E., Zelzer, E., Fratzl, P., Shahar, R., 2009. Mechanical function of a complex three-dimensional suture joining the bony elements in the shell of the red-eared slider turtle. Adv. Mater. 407–412.

Lakes, R., 1993. Materials with structural hierarchy. Nature 361, 511–515.

Lee, N., Horstemeyer, M.F., Rhee, H., Nabors, B., Liao, J., Williams, L.N., 2014. Hierarchical multiscale structure–property relationships of the red-bellied woodpecker (*Melanerpes carolinus*) beak. J. R. Soc. Interface 11.

Li, Y.N., Ortiz, C., Boyce, M., 2011. Stiffness and strength of suture joints in nature. Phys. Rev. E 84.

Li, Y.N., Ortiz, C., Boyce, M., 2012. A bio-inspired mechanical, deterministic fractal model for hierarchical suture joints. Phys. Rev. E 85.

Li, Y.N., Ortiz, C., Boyce, M., 2013. A generalized mechanical model for suture interfaces of arbitrary geometry. J. Mech. Phys. Solids 1144–1167.

Lin, E., Li, Y., Ortiz, C., Boyce, M.C., 2014. 3D printed, bio-inspired prototypes and analytical models for structured suture interfaces with geometrically- tuned deformation and failure behavior. J. Mech. Phys. Solids 73, 166–182.

Liu, L., Jiang, Y., Boyce, M., Ortiz, C., Baur, J., Song, J., Li, Y., 2017. The effects of morphological irregularity on the mechanical behavior of interdigitated biological sutures under tension. J. Biomech. 58, 71–78.

Liu, J., Wei, X., 2021. A universal fracture analysis framework for staggerd composites composed of tablets with different wavy topologies. J. Mech. Phys. Solids 151.

Lu, H., Zhang, J., Wu, N., Liu, K.B., Xu, D., Li, Q., 2009. Phytoliths analysis for the discrimination of Foxtail millet (*Setaria italica*) and common millet (*Panicum miliaceum*). PLoS One 4.

Malik, I.A., Barthelat, F., 2016. Toughening of thin ceramic plates using bioinspired surface patterns. Int. J. Solids Struct. 389–399.

Malik, I.A., Mirkhalaf, M., Barthelat, F., 2017. Bio-inspired jigsaw-like interlocking sutures: Modeling, optimization, 3D printing and testing. J. Mech. Phys. Solids 102, 224–238.

Moazen, M., Curtis, N., Higgins, P.O., Jones, M.E., Evans, S.E., Fagan, M.J., 2009. Assessment of the role of sutures in a lizard skull: a computer modelling study. Proc. Biol. Sci. 215, 642–655.

Pérez-Claros, J.A., Palmqvist, P., Olóriz, F., 2002. First and second orders of suture complexity in ammonites: a new methodological approach using fractal analysis. Math. Geol. 34, 323–343.

Pritchard, J.J., Scott, J.H., Girgis, F.G., 1956. The structure and development of cranial and facial sutures. J. Anat. 90, 73–86.

Pritz, T., 2007. The Poisson's loss factor of solid viscoelastic materials. J. Sound Vib. 306, 790–802.

Rayfield, E.J., 2004. Cranial mechanics and feeding in Tyrannosaurus rex. Proc. R. Soc. Lond. Biol. 271, 1451–1459.

Saunders, W.B., 1999. Evolution of complexity in paleozoic ammonoid sutures. Science 286, 760–763.

Song, J., Reichert, S., Kallai, I., Gazit, D., Wund, M., Boyce, M.C., Ortiz, C., 2010. Quantitative microstructural studies of the armor of the marine threespine stickleback (*Gasterosteus aculeatus*). J. Struct. Biol. 1–14.

Sun, Y., Wang, B., Pugno, N., Wang, B., Ding, Q., 2015. In-plane stiffness of the anisotropic multifunctional hierarchical honeycombs. Compos. Struct. 131, 616–626.

Wang, Q., Smith, A.L., Strait, D.S., Wright, B.W., Richmond, B.G., Grosse, I.R., Byron, C.D., Zapata, U., 2010. The global impact of sutures assessed in a finite element model of a macaque cranium. Anat. Rec. 293, 1477–1491.

Yu, Z., Liu, J., Wei, X., 2020. Achieving outstanding damping performance through bio-inspired sutural tessellations. J. Mech. Phys. Solids.

Mechanical modelling of viscoelastic hierarchical suture joints and their optimization and auxeticity- Supplementary Material

F. Ongaro, N. M. Pugno

Different levels with different geometry

Table 1: *Different levels with different geometry: hierarchical configurations examined*

	level-[1]	level-[2]	level-[3]	level-[4]
TRA1	trapezoidal	triangular	rectangular	anti-trapezoidal
TRA2	trapezoidal	triangular	anti-trapezoidal	rectangular
TRA3	trapezoidal	rectangular	triangular	anti-trapezoidal
TRA4	trapezoidal	rectangular	anti-trapezoidal	triangular
TRA5	trapezoidal	anti-trapezoidal	triangular	rectangular
TRA6	trapezoidal	anti-trapezoidal	rectangular	triangular
TRA7	trapezoidal	trapezoidal	trapezoidal	trapezoidal
REC1	rectangular	triangular	trapezoidal	anti-trapezoidal
REC2	rectangular	triangular	anti-trapezoidal	trapezoidal
REC3	rectangular	trapezoidal	triangular	anti-trapezoidal
REC4	rectangular	trapezoidal	anti-trapezoidal	triangular
REC5	rectangular	anti-trapezoidal	triangular	trapezoidal
REC6	rectangular	anti-trapezoidal	trapezoidal	triangular
REC7	rectangular	rectangular	rectangular	rectangular
ANTI1	anti-trapezoidal	triangular	trapezoidal	rectangular
ANTI2	anti-trapezoidal	triangular	rectangular	trapezoidal
ANTI3	anti-trapezoidal	trapezoidal	triangular	rectangular
ANTI4	anti-trapezoidal	trapezoidal	rectangular	triangular
ANTI5	anti-trapezoidal	rectangular	triangular	trapezoidal
ANTI6	anti-trapezoidal	rectangular	trapezoidal	triangular

ANTI7 anti-trapezoidal anti-trapezoidal anti-trapezoidal anti-trapezoidal

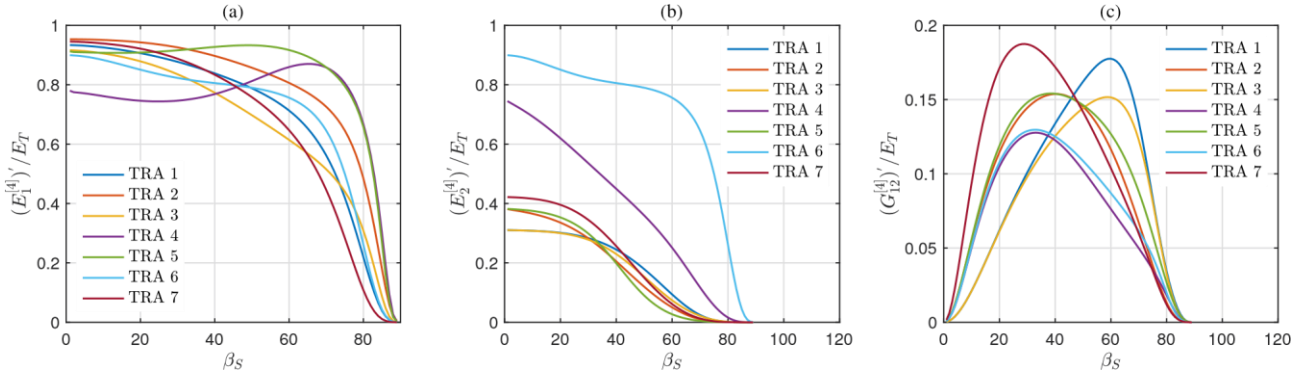

Figure 1:*a trapezoidal pro Influence of the tooth tip angle file at the first level: (a) ϐs into the effective stiffness of hierarchical sutures having* $(E_{1[4]})' /E_T$, *(b)* $(E_{2[4]})' /E_T$, *(c)* $(G_{12[4]})' /E_T$.

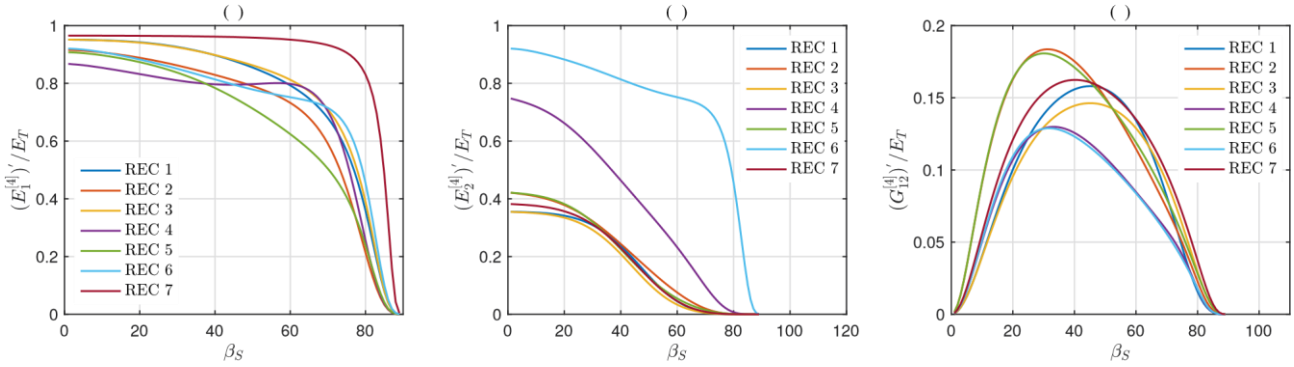

Figure 2:*a rectangular pro Influence of the tooth tip angle file at the first level: (a) ϐs into the effective stiffness of hierarchical sutures having* $(E_{[4]})' /E_T$, *(b)* $(E_{2[4]})' /E_T$, *(c)* $(G_{12[4]})' /E_T$.

1

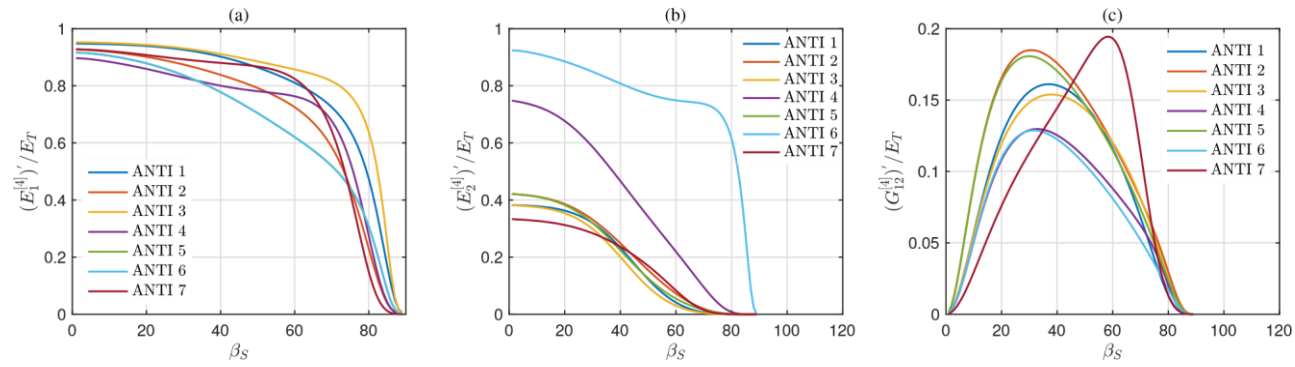

Figure 3:*an anti-trapezoidal pro Influence of the tooth tip angle file at the first level: (a) ϐs into the effective stiffness of hierarchical sutures having* $(E_{1[4]})$, $/E_T$, *(b)* $(E_{2[4]})$, $/E_T$, *(c)* $(G_{12[4]})$, $/E_T$.

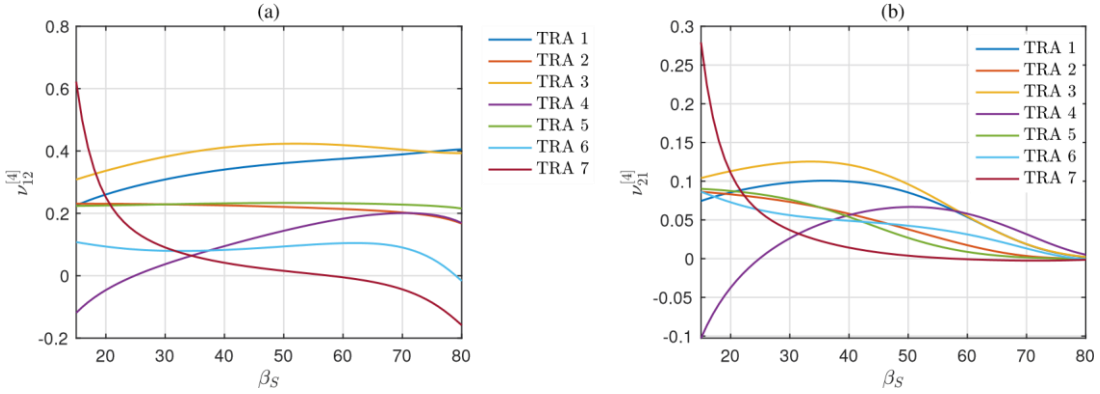

Figure 4: *Insutures having a trapezoidal profluence of the tooth tip angle ϐs into the effective Poisson's ratios of hierarchical file at the first level: (a)* $v_{12[4]}$, *(b)* $v_{21[4]}$.

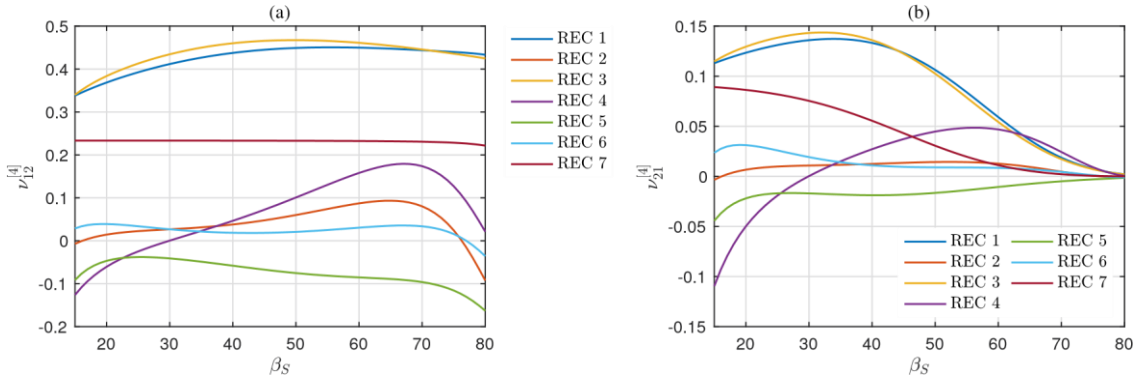

Figure 5: *Insutures having a rectangular profluence of the tooth tip angle ϐs into the effective Poisson's ratios of hierarchical file at the first level: (a)* $v_{12[4]}$, *(b)* $v_{21[4]}$.

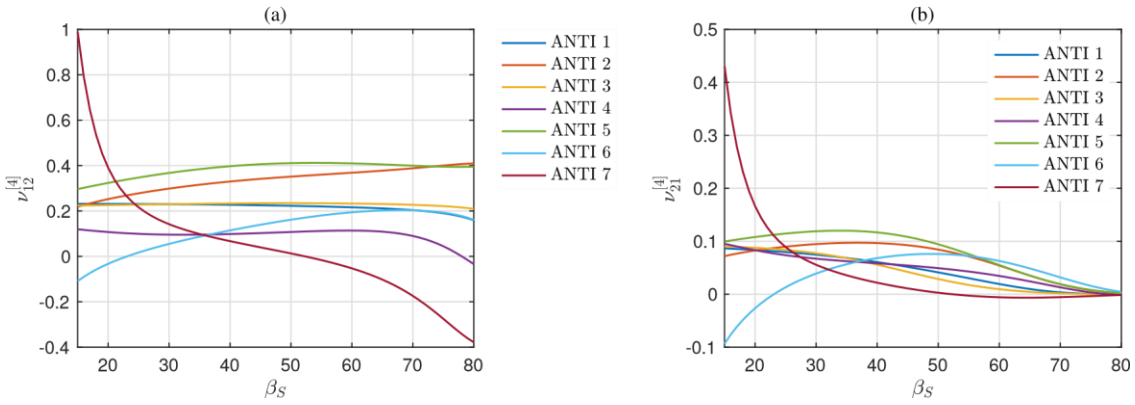

Figure 6:sutures having an anti-trapezoidal pro Influence of the tooth tip angle ϐs into the effective Poisson's ratios of hierarchical file at the first level: (a) $\nu_{12[4]}$, (b) $\nu_{21[4]}$.

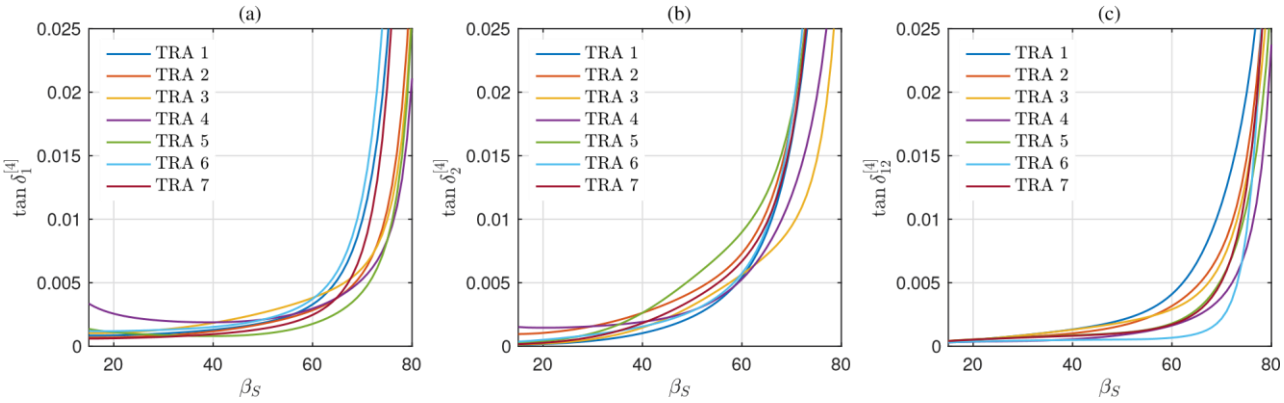

Figure 7: Infltrapezoidal prouence of the tooth tip angle file at the first level: (a) ϐs into the loss tangent of hierarchical sutures having a $\tan_{1[4]}$, (b) $\tan\delta_{2[4]}$, (c) $\tan\delta_{12[4]}$. δ

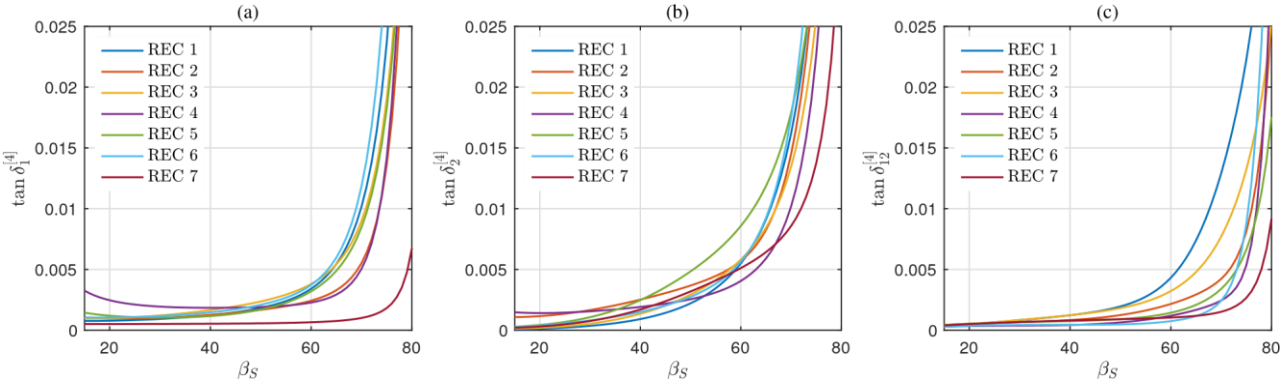

Figure 8: *Inflrectangular prouence of the tooth tip angle file at the first level: (a) ϐs into the loss tangent of hierarchical sutures having a tan* $_{1[4]}$*, (b) tan*$\delta_{2[4]}$*, (c) tan*$\delta_{12[4]}$*.* δ

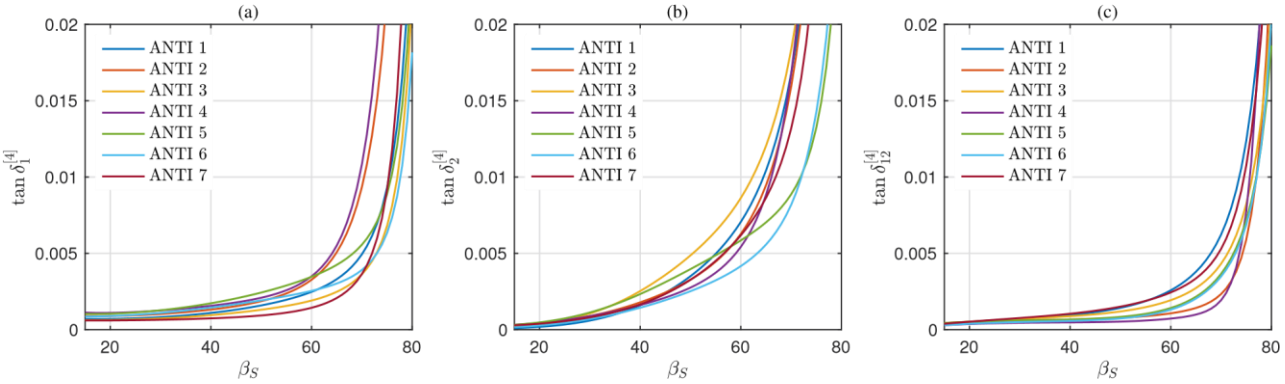

Figure 9: *Inanti-trapezoidal profluence of the tooth tip angle file at the fiϐrst level: (a)* $_s$ *into the loss tangent of hierarchical sutures having an tan* $_{1[4]}$*, (b) tan*$\delta_{2[4]}$*, (c) tan*$\delta_{12[4]}$*.*

δ